CrossMark

Linking Atmospheric Chemistry of the Hot Jupiter HD 209458b to Its Formation Location through Infrared Transmission and Emission Spectra

Spandan Dash[1,2,3] , Liton Majumdar[2,3] , Karen Willacy[4] , Shang-Min Tsai[5] , Neal Turner[4] , P. B. Rimmer[6,7,8] ,
Murthy S. Gudipati[4] , Wladimir Lyra[9] , and Anil Bhardwaj[10]
[1] Department of Physics, University of Warwick, Coventry, West Midlands, CV4 7AL, UK; dashspandan@gmail.com
[2] School of Earth and Planetary Sciences, National Institute of Science Education and Research, Jatni 752050, Odisha, India; dr.liton.majumdar@gmail.com
[3] Homi Bhabha National Institute, Training School Complex, Anushaktinagar, Mumbai 400094, India
[4] Jet Propulsion Laboratory, California Institute of Technology, 4800 Oak Grove Drive, Pasadena, CA 91109, USA
[5] Atmospheric, Ocean, and Planetary Physics, Department of Physics, University of Oxford, Oxford, OX1 3PU, UK
[6] MRC Laboratory of Molecular Biology, Francis Crick Avenue, Cambridge CB2 0QH, UK
[7] Astrophysics Group Cavendish Laboratory, JJ Thomson Avenue, Cambridge CB3 0HE, UK
[8] Department of Earth Sciences, University of Cambridge, Downing Street, Cambridge CB2 3EQ, UK
[9] Department of Astronomy, New Mexico State University, PO BOX 30001, MSC 4500, Las Cruces, NM 88003-8001, USA
[10] Physical Research Laboratory, Ahmedabad, 380009, India
Received 2021 July 17; revised 2022 March 28; accepted 2022 April 6; published 2022 June 10

Abstract

The elemental ratios of carbon, nitrogen, and oxygen in the atmospheres of hot Jupiters may hold clues to their formation locations in the protostellar disk. In this work, we adopt gas-phase chemical abundances of C, N, and O from several locations in a disk chemical kinetics model as sources for the envelope of the hot Jupiter HD 209458b and evolve the atmospheric composition of the planet using a 1D chemical kinetics model, treating both vertical mixing and photochemistry. We consider two atmospheric pressure-temperature profiles, one with and one without a thermal inversion. From each of the resulting 32 atmospheric composition profiles, we find that the molecules CH_4, NH_3, HCN, and C_2H_2 are more prominent in the atmospheres computed using a realistic noninverted P–T profile in comparison to a prior equilibrium chemistry based work, which used an analytical P–T profile. We also compute the synthetic transmission and emission spectra for these atmospheres and find that many spectral features vary with the location in the disk where the planetary envelope was accreted. By comparing with the species detected using the latest high-resolution ground-based observations, our model suggests that HD 209458b could have accreted most of its gas between the CO_2 and CH_4 ice lines with a supersolar C/O ratio from its protostellar disk, which in turn directly inherited its chemical abundances from the protostellar cloud. Finally, we simulate observing the planet with the James Webb Space Telescope (JWST) and show that differences in spectral signatures of key species can be recognized. Our study demonstrates the enormous importance of JWST in providing new insights into hot-Jupiter formation environments.

Unified Astronomy Thesaurus concepts: Exoplanet atmospheres (487); Protoplanetary disks (1300)

1. Introduction

The detection of the Na doublet at 589.3 nm in the atmosphere of HD 209458b (Charbonneau et al. 2002) heralded the era of atmospheric characterization of exoplanets and confirmed theoretical predictions made by Seager & Sasselov (2000), Brown (2001), and Hubbard et al. (2001). This was followed by the discovery of an extended atmosphere on the same planet with the detection of H I, O I, and C II in the escaping upper atmosphere beyond the Roche lobe (Vidal-Madjar et al. 2003, 2004). The source of H I was almost immediately explained by a simple hydrogen- and oxygen-based photochemical model by Liang et al. (2003). Since then, more observations have resulted in the detection of simple molecules such as H_2O, CO, CH_4, HCN, and NH_3 in the atmosphere of HD 209458b (Swain et al. 2009; Snellen et al. 2010; Sing et al. 2016; Tsiaras et al. 2016, 2018; MacDonald & Madhusudhan 2017; Brogi & Line 2019; Sánchez-López et al. 2019; Giacobbe et al. 2021). Chemical models to explain spectral observations have kept pace with both chemical

equilibrium, e.g., TEA (Blecic et al. 2016) and FastChem (Stock et al. 2018), as well as chemical kinetics models, e.g., Zahnle et al. (2009), KINETICS (Moses et al. 2011, 2013a, 2013b), the Kasting model (Kopparapu et al. 2012), the Venot model (Venot et al. 2012), ATMO (Amundsen et al. 2014; Drummond et al. 2016), VULCAN (Tsai et al. 2017), ARGO (Rimmer & Helling 2016), and LEVI (Hobbs et al. 2019), using better and more precise networks of chemical reactions aided by new and/or improved laboratory data as well as observations.

Formation conditions and evolution history of exoplanets can be potentially linked to their C/O and N/O ratios (Öberg et al. 2011; Eistrup et al. 2016; Mordasini et al. 2016; Ali-Dib 2017; Eistrup et al. 2018; Cridland et al. 2019a; Notsu et al. 2020; Nowak et al. 2020; Hobbs et al. 2021b; Turrini et al. 2021). For giant planets formed by the core accretion mechanism, the core is thought to be formed by accretion of solid ice material from the disk midplane in a core accretion or pebble accretion stage or a hybrid mix of both (Alibert et al. 2018), and the envelope is thought to be formed by rapid/runaway accretion of gas from the local gas disk region close to the disk midplane after the formation of their cores (Eistrup et al. 2016; Notsu et al. 2020). Envelope accretion uses gas that is available vertically for at least 1 scale height (Tanigawa et al. 2012; Morbidelli et al. 2014;

Teague et al. 2019) from the disk midplane, and Cridland et al. (2020) found that planets formed within 20 au would reflect the C/O ratio of the gas accreted during this stage. The rapid gas accretion timescale is also much smaller than the Type-II migration timescale required for the cores to migrate inward (Pollack et al. 1996), and hence almost all the gas in the planetary envelope is accreted very close to where its runaway accretion starts.

Local gas-phase and grain abundances of elements such as C, O, and N differ in the radial direction, as shown by disk midplane chemistry models (Öberg et al. 2011; Eistrup et al. 2016, 2018). In a simplified scenario, these radially varying profiles of elemental abundances will then serve as the initial conditions for the further evolution of the core as well as the envelope. Hence, looking at the evolution of such a gaseous envelope has the potential to link an exoplanet at the very least to the location where it accreted the majority of its gaseous envelope. However, in a more realistic sense, the envelope itself can be contaminated by accretion of more icy planetesimals or comets and asteroids, or it may even be affected by degassing from the differentiating and partitioning core. All these processes can then muddle the entire scenario, such that it becomes very difficult to determine a direct connection of chemistry of gas giant atmospheres with the disk chemistry at the location where they formed. In this work, we assume the earlier simpler case, but we discuss the effect of disk solid contamination as a limitation of the model (see Section 4.3) and consider one possible model of contamination from Turrini et al. (2021) and find the effect it can have on spectra. The simpler case has also been assumed by previous works, which include disk chemistry in planet formation and atmospheric evolution models (Cridland et al. 2017, 2019a, 2019b, 2020; Booth & Ilee 2019). However, all their models had a limited set of chemical networks or used networks of an equivalent complexity as Eistrup et al. (2016). This motivates us to use the results from Eistrup et al. (2016) as the starting point for our analysis.

Mordasini et al. (2016) modeled the effect of disk chemistry on simulated James Webb Space Telescope (JWST) and ARIEL spectral signatures of hot Jupiters using the concept outlined above in a planetesimal accretion regime, with the final atmospheric composition being enriched by planetesimal impacts during formation. They found that their hot Jupiters could be divided into "dry" or "wet", depending on a formation inside or outside the water ice line, respectively. Both types were depleted in C and enriched in O as the standard inner disk chemistry model assumed by them was already depleted in C. This resulted in dry planets with C/O ratios lower than 0.2 and wet planets with C/O ratios of 0.1–0.5, respectively. They also found differences in their modeled JWST and ARIEL spectra for the extreme cases of dry and wet hot Jupiters. C/O ratios greater than 1 for planets were only possible for dry hot Jupiters if the disk chemistry was assumed to be nonstandard with no refractory C depletion. However, without knowledge of how this could happen, it was difficult to find formation locations of hot Jupiters that show evidence of high (including supersolar) atmospheric C/O ratios, e.g., HD 209458b (Giacobbe et al. 2021). Nonetheless, the basis of linking exoplanet composition through transmission and emission spectra to disk chemistry still remains important and forms a major basis of this work.

Eistrup et al. (2016) presented the case for including detailed gas-phase and grain networks to evolve the chemistry of gas and ice in disk midplanes and found that the results for the radially varying gaseous elemental abundance profiles of CO, CO_2, H_2O, NH_3, N_2, O_2, and CH_4 were more diverse. Using this as basis, Notsu et al. (2020) for the first time presented cases of model hot-Jupiter atmospheric chemistry starting from gas-phase elemental abundances obtained from such disk chemistry models (within the limit of 20 au provided in Cridland et al. 2020) and found cases with gas-phase envelope C/O ratios greater than supersolar and >1 as well. They assumed that local gas accretion occurs for a migrating hot Jupiter in a narrow region in between various ice lines (H_2O, CO_2, CH_4, and CO) and hence the elemental abundances of C/H, O/H, N/H, and the overall C/O ratios would be an indicator of the formation location of a hot Jupiter. However, they did not look at how changes in initial elemental abundances based on disk location might produce detectable observational spectral signatures.

Following the potential evidence in Mordasini et al. (2016) that the JWST and ARIEL can be used to trace the composition in exoplanet atmospheres, we extend the work of Notsu et al. (2020) to do the same with one caveat: we simulate disequilibrium chemistry by including the effects of vertical mixing, diffusion, and photochemistry instead of just equilibrium chemistry. Moses (2014) noted that disequilibrium can greatly affect the levels of species such as HCN and C_2H_2 in the photosphere, which can produce detectable spectral signatures. This limitation about the usage of equilibrium over disequilibrium chemistry in their model was noted in Notsu et al. (2020). All these factors form the basis of our study.

More recently, Turrini et al. (2021) and Hobbs et al. (2021b) have also worked on tracing the history of planet formation through molecular markers. Turrini et al. (2021) have used initial gas and solids/ice abundances gleaned from a sophisticated analysis of meteoritic abundances, interstellar medium (ISM) abundances, and astrochemical model abundances from Eistrup et al. (2016) and Eistrup et al. (2018). However, they have only focused on the inheritance with a low-ionization case (see Section 2.3 for an overview of the cases). We have used the reset (atomic) and inheritance (molecular) inputs, with both high- and low-ionization rates in this work. Hobbs et al. (2021b) used a large grid of initial C/H, O/H, and N/H abundances and P–T-K_{zz} profiles to evolve their exoplanetary atmosphere using the chemical kinetics code LEVI and then compared the range of resultant molecular abundance values of H_2O, CO, CH_4, CO_2, HCN, and NH_3 to the possible initial abundance values predicted by different planet formation, enrichment, and migration models. In comparison, our study is restricted to only one possible planet formation and migration pathway. However, the chemistry from Woitke et al. (2009) is based on chemical equilibrium in the disk midplane as opposed to the time-dependent chemical kinetics of Eistrup et al. (2016). Hobbs et al. (2021b) have also used the initial abundance values used in Turrini et al. (2021), but as we pointed out earlier, it is only for the case of inheritance with low ionization. However, neither of the two studies directly looked at the possibility of linking spectra to the chemistry in the protostellar disk.

In this paper, we consider the specific case of exoplanet HD 209458b and consider two different P–T profiles (with and without a temperature inversion). We use a custom-built
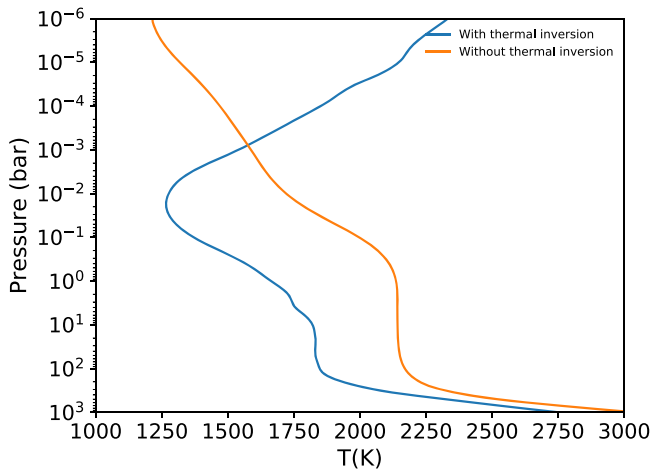
Figure 1. The two *P–T* profiles used in this study. For the case of thermal inversion, the *P–T* profile is as used in Moses et al. (2011), and for the noninverted case, the temperature profile is calculated using the open-source self-consistent radiative transfer code HELIOS, using the planetary parameters for HD 209458b and solar spectrum as an analogue.

wrapper that couples the 1D chemical kinetics code VULCAN (Tsai et al. 2017, 2021; in order to simulate disequilibrium chemistry by incorporating vertical transport, diffusion, and photochemistry) with the radiative transfer package petitRAD-TRANS (Mollière et al. 2019; to create synthetic transmission and emission spectra). We vary the initial elemental abundances based on the values provided in Notsu et al. (2020) for gas accretion at specific radial positions in the disk and determine if the differences in the constructed transmission and emission spectra could be an indicator of its C/O ratio and/or where the exoplanet could have accreted most of its gas from the disk.

2. Methods

2.1. Physical Structure of HD 209458b

HD 209458b was the first exoplanet to be discovered using the transit method. It orbits a 1.203 $R_\odot$ (Boyajian et al. 2015) and 1.148 $M_\odot$ (Southworth 2010) star situated 47 pc away. Since these stellar parameter values are very close to the values used by Notsu et al. (2020), we chose HD 209458 as a viable candidate for this study. Additionally, the mass of HD 209458b is 0.69 M_J, the radius is 1.38 R_J, and the orbital radius is 0.04747 au (Southworth 2010).

The *P–T* profile of this planet has been subject to debate, with Burrows et al. (2007) and Knutson et al. (2008) initially suggesting the existence of a thermal inversion in the atmosphere. However, more recently, Diamond-Lowe et al. (2014) and Line et al. (2016) have obtained evidence against a thermal inversion being present between 1 bar to 10^{-3} bar. Given this uncertainty, we use two *P–T* profiles, one with and one without thermal inversion. Both *P–T* profiles are shown in Figure 1.

The profile with a thermal inversion is taken from Figure 2 of Moses et al. (2011), and for this model, we also use the pressure-K_{zz} profile from the same paper (see Figure 1 of Moses et al. 2011). The profile without the inversion is constructed using the open-source self-consistent radiative transfer code for exoplanet atmospheres called HELIOS[11] (Malik et al. 2017) by

considering H_2O, CH_4, CO, CO_2, NH_3, HCN, C_2H_2, NO, SiH, CaH, MgH, NaH, AlH, CrH, AlO, SiO, CaO, Na, K, and H- as sources of opacities in the atmosphere. In addition, CIA opacities for H_2–H_2 and H_2–He were used. This profile is different from the noninverted *P–T* profile adopted by Notsu et al. (2020), who calculated it using the analytical *P–T* formula from Guillot (2010). Notably, our *P–T* profile is cooler at a pressure $>10^2$ bar, hotter over the range of 10^2–10^{-4} bar, and cooler at pressures $<10^{-4}$ bar. Our non-inverted *P–T* profile is slightly hotter than the one presented in Lavvas & Arfaux (2021) since we have used a heat re-distribution factor (f) of 2/3 to represent the dayside in a poor heat-redistribution case (Komacek & Showman 2016).

To generate synthetic transmission spectra, a reference photospheric pressure is also needed. We use a nominal value of atmospheric pressure at the photosphere (P_{ref}) = 10^{-2} bar or 10 mbar. This is about three times higher than the value obtained by MacDonald & Madhusudhan (2017), who found the photosphere to lie at a mean value of $10^{-2.45}$ bar using retrieval from transmission spectrum observations.

2.2. Chemical Evolution and Spectra

We use a custom-built Python3 wrapper that couples a chemical kinetics code (VULCAN) with a radiative transfer code (petitRADTRANS) to obtain transmission and emission spectra for any exoplanet of interest. We use the open-source 1D chemical kinetics model VULCAN[12] as the first part of this package to evolve the atmospheric chemistry for HD 209458b. We use the default NCHO network provided in the original repository, which tracks over 600 reactions linking 50 species (Zilinskas et al. 2020). We include eddy diffusion (K_{zz}), molecular diffusion, and photochemistry while running all simulations, effectively using disequilibrium chemistry for our exoplanet candidate. For the stellar flux, we use the default flux file for the Sun provided in the original repository (Gueymard solar flux file) as both our Sun and HD 209458 are G-type stars with similar mass and radius parameters.

For the NCHO network, VULCAN uses specific elemental abundances for N, C, O, and He with respect to H in order to first calculate the initial atmospheric molecular mixing ratios using the coupled equilibrium chemistry code FastChem[13] (Stock et al. 2018). We retain the abundance of He with respect to H as 0.097 (Asplund et al. 2009; Tsai et al. 2017) and change the others to values that we discuss in Section 2.3. They are listed in Table 1.

We use the open-source radiative transfer package peti-tRADTRANS[14] (Mollière et al. 2019) to obtain synthetic transmission and emission spectra. Apart from using the stellar and planetary parameters as provided in Section 2.1, we use line opacities of H_2, CO, CO_2, CH_4, H_2O, HCN, NH_3, C_2H_2, and CN. In addition, we include collision-induced absorption (CIA) opacities for H_2–H_2 and H_2–He and Rayleigh scattering for H_2 and He. All of these are already present in the default latest version of petitRADTRANS. We run petitRADTRANS in the default *c-k* (i.e., correlated-k) mode, and hence our synthetic spectra have a resolution of $R = 1000$. For the emission spectra, we use a synthetic PHOENIX stellar spectrum of $T_{eff} = 6092$ K (Boyajian et al. 2015), which is

---

[11] https://github.com/exoclime/HELIOS

[12] https://github.com/exoclime/VULCAN
[13] https://github.com/exoclime/FastChem
[14] https://petitradtrans.readthedocs.io/en/latest/

Table 1
Input Parameters Used to Run Each Atmospheric Model with the First Horizontal Line Separating Molecular Initial Abundances above from Atomic Initial Abundances below

Model	Location (au)	Ionization	C/H	O/H	N/H	C/O[a]	C/N	Initial abundances
A1/A2	0.5	low	1.81×10^{-4}	5.20×10^{-4}	6.24×10^{-5}	0.35	2.90	Molecular
B1/B2	1.0	low	1.67×10^{-4}	2.07×10^{-4}	6.24×10^{-5}	0.81	2.68	Molecular
C1/C2	5.0	low	7.06×10^{-5}	5.57×10^{-5}	4.18×10^{-5}	1.27	1.69	Molecular
D1/D2	20.0	low	5.40×10^{-5}	5.37×10^{-5}	4.14×10^{-5}	1.00	1.30	Molecular
E1/E2	0.5	high	1.80×10^{-4}	5.19×10^{-4}	6.24×10^{-5}	0.35	2.90	Molecular
F1/F2	1.0	high	1.81×10^{-4}	2.20×10^{-4}	6.24×10^{-5}	0.82	2.90	Molecular
G1/G2	5.0	high	1.76×10^{-5}	1.87×10^{-5}	4.68×10^{-5}	0.94	0.38	Molecular
H1/H2	20.0	high	3.07×10^{-6}	3.07×10^{-6}	3.99×10^{-5}	1.00	0.08	Molecular
I1/I2	0.5	low	1.81×10^{-4}	5.21×10^{-4}	6.24×10^{-5}	0.35	2.90	Atomic
J1/J2	1.0	low	1.81×10^{-4}	5.17×10^{-4}	6.24×10^{-5}	0.35	2.90	Atomic
K1/K2	5.0	low	3.16×10^{-5}	2.37×10^{-4}	5.65×10^{-5}	0.13	0.56	Atomic
L1/L2	20.0	low	6.19×10^{-6}	1.51×10^{-5}	2.43×10^{-5}	0.41	0.25	Atomic
M1/M2	0.5	high	1.81×10^{-4}	5.21×10^{-4}	6.24×10^{-5}	0.35	2.90	Atomic
N1/N2	1.0	high	1.81×10^{-4}	5.19×10^{-4}	6.24×10^{-5}	0.35	2.90	Atomic
O1/O2	5.0	high	8.16×10^{-5}	3.25×10^{-4}	5.82×10^{-5}	0.25	1.40	Atomic
P1/P2	20.0	high	3.90×10^{-6}	4.36×10^{-6}	2.34×10^{-5}	0.89	0.17	Atomic
T1	5	low	2.8×10^{-4}	5.7×10^{-4}	7.6×10^{-5}	0.49	3.64	Molecular
T2	12	low	4×10^{-4}	6.9×10^{-4}	8.1×10^{-5}	0.58	4.95	Molecular
T3	19	low	5.3×10^{-4}	1×10^{-3}	1×10^{-4}	0.53	5.31	Molecular
T4	50	low	9.7×10^{-4}	2×10^{-3}	1.4×10^{-4}	0.50	6.80	Molecular
T5	100	low	1.4×10^{-3}	2.8×10^{-3}	1.8×10^{-4}	0.50	7.54	Molecular
T6	130	low	2.2×10^{-3}	4.5×10^{-3}	2.7×10^{-4}	0.50	8.28	Molecular

Notes. Each model corresponds to an alphabet running from A to P, and 1 or 2 represent use of a thermally inverted or a nonthermally inverted P–T profile, respectively. The models after the second horizontal line are the initial abundances from Table 4 of Turrini et al. (2021), representing atmospheric enrichment by solids.
[a] Solar C/O is 0.55 (Asplund et al. 2009). Accordingly, in this paper we have used subsolar and supersolar nomenclature for C/O values lower and greater than this value.

constructed using the default PHOENIX spectrum calculator in petitRADTRANS.

2.3. Elemental Abundances

We use the 16 values of elemental gas-phase C/H, O/H, and N/H abundances listed in Table 1 in Notsu et al. (2020). All these were derived from the midplane disk chemistry model of Eistrup et al. (2016), which incorporates gas-phase, gas-grain chemistry and grain surface chemistry and is evolved until 1 Myr to obtain these results. The ice-line locations for H_2O, CO, CH_4, and CO_2 are assumed to lie at 0.7, 2.6, 16, and 26 au, corresponding to temperatures of 177, 88, 28, and 21 K, respectively. As with Notsu et al. (2020), we have also listed the initial elemental abundance values corresponding to different radial distances in the disk (0.5, 1, 5, and 20 au, corresponding to positions interior to the H_2O ice line, between the H_2O and CO_2 ice lines, between the CO_2 and CH_4 ice lines, and between the CH_4 and CO ice lines, respectively) in Table 1.

The first eight values in Table 1 are abundances of C, O, and N with respect to H in a case where the disk wholly inherits the chemistry from the protostellar cloud (inheritance scenario, called "molecular initial abundances"), and the second part of the table is the case where the chemistry in the disk gas can be altered significantly from the initial protostellar cloud (Visser et al. 2015) due to heating events generated from the protostar (e.g., stellar irradiation, accretion bursts, or shocks generated during protostellar formation stage). Eistrup et al. (2016) posited that an extreme case of this alteration could convert all

molecules into atoms within 30 au, which will then subsequently reform into molecules and solids in a condensation sequence. Hence, this case is called the reset scenario, or "atomic initial abundances". Both situations represent two extreme positions for the initial chemical abundances of a disk that formed from the collapse of a protostellar cloud. A realistic situation is hence expected to lie in between these two cases.

Each case is further subdivided into subcases where the disk is under low ($\zeta < 10^{-18}$) or high ($\zeta \sim 10^{-17}$) values of ionization, corresponding to a low and high level of chemical processing in the disk, respectively. The low-ionization condition only takes into account ionization from short-lived decay products of radio nucleotides inside the disk itself. The high value of ionization takes into account the previous source as well as cosmic-ray ionization external to the disk. The first case produces a higher level of ionization in the inner disk than in the outer disk, and the second case has a higher level of ionization in the outer disk than in the inner disk. Which case works in a disk ultimately depends on how much the disk is shielded by solar flares and magnetic fields from external cosmic rays (Eistrup et al. 2016).

For the case of molecular initial abundances with low ionization in Table 1, the gas-phase C/O ratio increases from the inner disk to the outer disk as the various ice lines are crossed. This is very similar to the step-wise C/O distribution in Öberg et al. (2011) and shows that this case shows the minimum effect of chemical processing in the disk. The case for molecular initial abundances with high ionization in the same table also shows the same behavior, except for a

difference between the CO and CH_4 ice lines at 5 au, where the C/O ratio is now subsolar (0.94 versus 1.27 for the previous case). This is because C/H is depleted further due to CO beyond 2 au and CH_4 between 1 and 16 au in the gas phase are destroyed by increased ionization, and the resulting grain surface reaction products CO_2, H_2CO and C_2H_6 are frozen out in the solid phase (Eistrup et al. 2016). This also has the effect of reducing the gas-phase O/H abundance. At 20 au, the overall C/H and O/H abundances are even more significantly depleted due to the freezing-out of CH_4 and O_2 (ice line at 21 au), in addition to the depletion causes already mentioned above. The dichotomy between the values of N/H at 0.5–1 au and 5–20 au for both cases arises because the NH_3 ice line lies at 2.5 au. However, N_2 in the gaseous phase is still more than enough for all the values to remain similar within the same order of magnitude.

The C/O ratio behavior is very different for the two subcases of atomic initial abundances in Table 1. It is because in this case, the disk chemistry starts from atoms, and the formation of gas-phase molecules at a particular location depends on the corresponding temperature and ionization conditions. At radius >0.3 au, CO and O_2 are the main C- and O-carrying molecules, and N_2 is the main N-carrying molecule. CH_4 is almost completely depleted compared to the inheritance scenario. Therefore the C/O ratio generally remains subsolar for all the locations considered. At 5 au, the C/O ratio falls even further because of the CO-to-CO_2 ice conversion mechanism pointed out above, which depletes the gas-phase C/H. The C/O is highest at 20 au because here, the gas-phase O_2 starts freezing out.

All 32 input values (16 for each P–T profile) for elemental abundances with model labels, location, presence of an inversion in the P–T profile, ionization, and C/O ratio details are summarized in Table 1. Each set of three abundances (C/H, O/H, and N/H) is assumed to be the starting initial elemental abundances for the gas accreted onto the envelope of HD 209458b and then fed into VULCAN as initial elemental abundances in order to evolve the chemistry of its atmosphere.

2.4. JWST Observation Simulation

We simulated JWST observations using the command-line version of the open-source PandExo (Batalha et al. 2017) package using a similar procedure as provided in Zilinskas et al. (2020). NIRISS cannot be used for HD 209458 as the star is brighter than the lower observing limit for saturation for this instrument, i.e., a J-band magnitude (in near-infrared transmission window) = 6.6 (Wenger et al. 2000) versus recommended lower limits of 7 for substrip 96 and 8 for substrip 256, respectively. We did not use NIRSpec either as HD 209458 is brighter than what can be observed (without saturation) using its prism mode and its brightness is close to the upper limit of brightness that can be observed using the grism modes, i.e., J-band magnitude = 6.6 versus a recommended lower limit of 6. The NIRCam grism F322W2 and F444W (using SUB-GRISM64 which has the fastest readout) and MIRI LRS (slitless) modes are used to simulate observations over 2.4 μm to 13 μm because the brightness of our source falls safely within the limits of both instruments, i.e., a K value of 6.3 (Wenger et al. 2000) versus a lower limit of saturation of 4 for MIRI. Noise levels of 30 ppm and 50 ppm were used for the two instruments, respectively (Zilinskas et al. 2020). A saturation limit of 80% of full-well capacity was specified,

and we chose four transits in total to simulate observations. These observations were later binned to a spectral resolution of $R = 100$ for four transits similar to Zilinskas et al. (2020; who used $R = 15$, however). The two modes of NIRcam grisms we have considered have an overlapping range of observation wavelengths with different sensitivities. Hence, we have retained the observations of F322W2 from 2.4–4 μm and of F444W from 4–5 μm to capture the best results from these instruments.

3. Results

We compare the atmospheric mixing ratios of all volatiles mentioned in Section 2.2 for the differing cases of molecular versus atomic initial abundances, levels of disk ionization (low or high), and P–T profiles (with and without a thermal inversion). We leave out H_2 and He as they dominate in all cases, but have little effect on the spectra beyond Rayleigh scattering and CIA. Following this, we then compare the differences in synthetic transmission and emission spectra for all these cases.

To aid in the analysis of the chemistry plots obtained from our models, we use the prescription provided in Tsai et al. (2018), who used Djikstra's algorithm in order to find the shortest path and the rate-limiting step (RLS) for a reaction converting one species into the other (see Appendix B of Tsai et al. 2018). We construct schematic plots for chemical pathways between CH_4–CO, CH_4–C_2H_2, CH_4–HCN, NH_3–HCN, and N_2–NH_3 at $P = 1$ mbar. Our choice of the pressure level was motivated by the fact that this pressure is close to the reference photospheric level we assume to probe the atmosphere and as it also represents the location where the noninverted P–T profile starts being cooler than the inverted P–T profile. Types of reaction pathways and the model-wise distribution of such pathways are covered in Figures 12–16 and Table 3, respectively, in the Appendix. This allows us to build comprehensive networks of chemical pathways connecting CH_4, CO, and HCN, and N_2, NH_3, and HCN, which we show in Figure 2 and which is the main plot for our pathway analysis below. Pathways are colored differently depending on their model and specific network dependence.

3.1. Trends in Atmospheric Mixing Ratios of Main Volatiles Under Different Elemental Abundances

3.1.1. For Molecular Initial Abundances

For the case of molecular initial abundances with low ionization with an atmospheric temperature inversion shown in panels (a), (b), (c), and (d) of Figure 3 (mixing ratios in solid lines for an inverted P–T profile) corresponding to models A1 to D1, the dominant volatile (apart from H_2 and He) in the atmosphere goes from H_2O for A1 to CO for B1 and then CH_4 for C1 and D1. Moving upward through the atmosphere (from 100 bar), the mixing ratio of H_2O typically falls before quenching at around a pressure level of 10 bars (for A1) or 1 bar (for B1 to D1) before it starts falling off in the upper atmosphere again ($<10^{-3}$ bar). The mixing ratio of H_2O at each level is set primarily by the balance between the destruction reactions $H+H_2O \rightarrow OH+H_2$ and $M+H_2O \rightarrow M+H+OH$ (where M is any other different species), and the formation reactions that are the reverse of these reactions. Both are fast for the case of a hot planet like HD 209458b, and hence the mixing ratios for H_2O remain close to equilibrium until it is
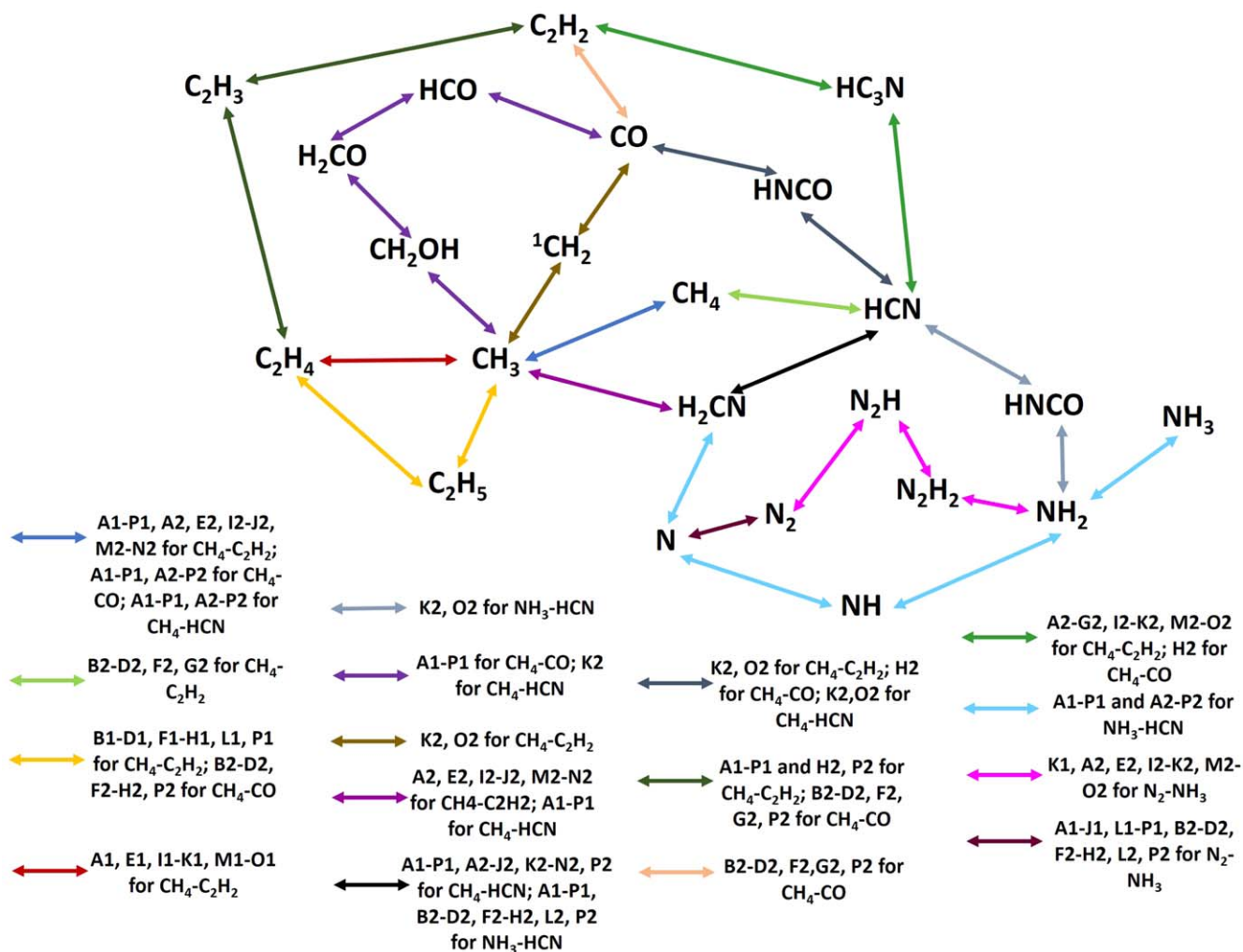
Dash et al.

Figure 2. Visualization of the major chemical pathways between a few selected molecules. All of these occur at $P = 1$ mbar. Note that HNCO has been depicted twice for better clarity. For individual model-wise reaction pathway analyses with addition of all secondary reactants, see Table 3 and Figures 12–16 in the Appendix.

quenched in the lower atmosphere, and this extends until millibar levels, at which point the destruction of of H_2O starts being important as the temperature exceeds 1900 K.

CO is the second most dominant volatile for panel a (A1) and third dominant (after CH_4 and N_2) for panels c and d (C1 and D1) and the most dominant volatile for panel b (model B1). The mixing ratio for CO increases as we move upward in the lower atmosphere before it quenches at around 10 bar and remains at that level. The mixing ratio for CO at each level is determined by a balance between its destruction primarily by the reactions $H+CO+M \rightarrow HCO+M$ and $CO+H_2 \rightarrow HCO + H$, and its formation by the reverse of these reactions. The first reaction is the main pathway in the CO-CH_4 interconversion for these atmospheric models indicated in Figure 2. For a hot planet like HD 209458b, both the forward and backward reactions are fast enough so that CO remains close to its equilibrium mixing ratio values and is quenched pretty low in the atmosphere, and it continues at this ratio until about microbar levels. The levels of both CO and H_2O in turn determine the mixing ratio of CO_2 in the atmosphere, with it being in a pseudo-equilibrium with both these species (Moses et al. 2011). Hence, as H_2O becomes depleted with increase in C/O, the mixing ratio of CO_2 also falls off accordingly. As would be apparent in Figure 2, CO is also responsible for the

levels of CH_4 and HCN in the atmosphere through the interconversion pathways. Hence, with the increase in C/O, the levels of both these species also increase.

The abundances of both H_2O and CO depend on the C/O ratio, with H_2O generally decreasing and CO generally increasing with the increase in C/O ratio. For C/O < 1, CO is generally the main C-carrying species and H_2O is the main O-carrying species. At a C/O = 0.5, these species have almost equal mixing ratios. For a subsolar C/O ratio, C would be the limiting element, and the abundance of CO would slightly decrease. With a supersolar C/O ratio, the availability of C becomes higher, and hence CO would typically increase in mixing ratio unless C is already heavily depleted in absolute abundance (panels (c) and (d) or models C1 and D1). With C/O > 1, O becomes the limiting element, and almost all O now ends up in CO, with H_2O being depleted.

The mixing ratio for CH_4 starts decreasing in the lower atmosphere before quenching in the mid-atmosphere (1 bar—1 mbar) before falling again in the upper atmosphere (<1 mbar). The mixing ratio at which CH_4 quenches increases with the C/O ratio due to an increased availability of C. The fall of the CH_4 levels above 1 mbar is due to the increased prominence of the two reaction pathways forming HCN (CH_4–HCN pathway for these models) and C_2H_2 by either

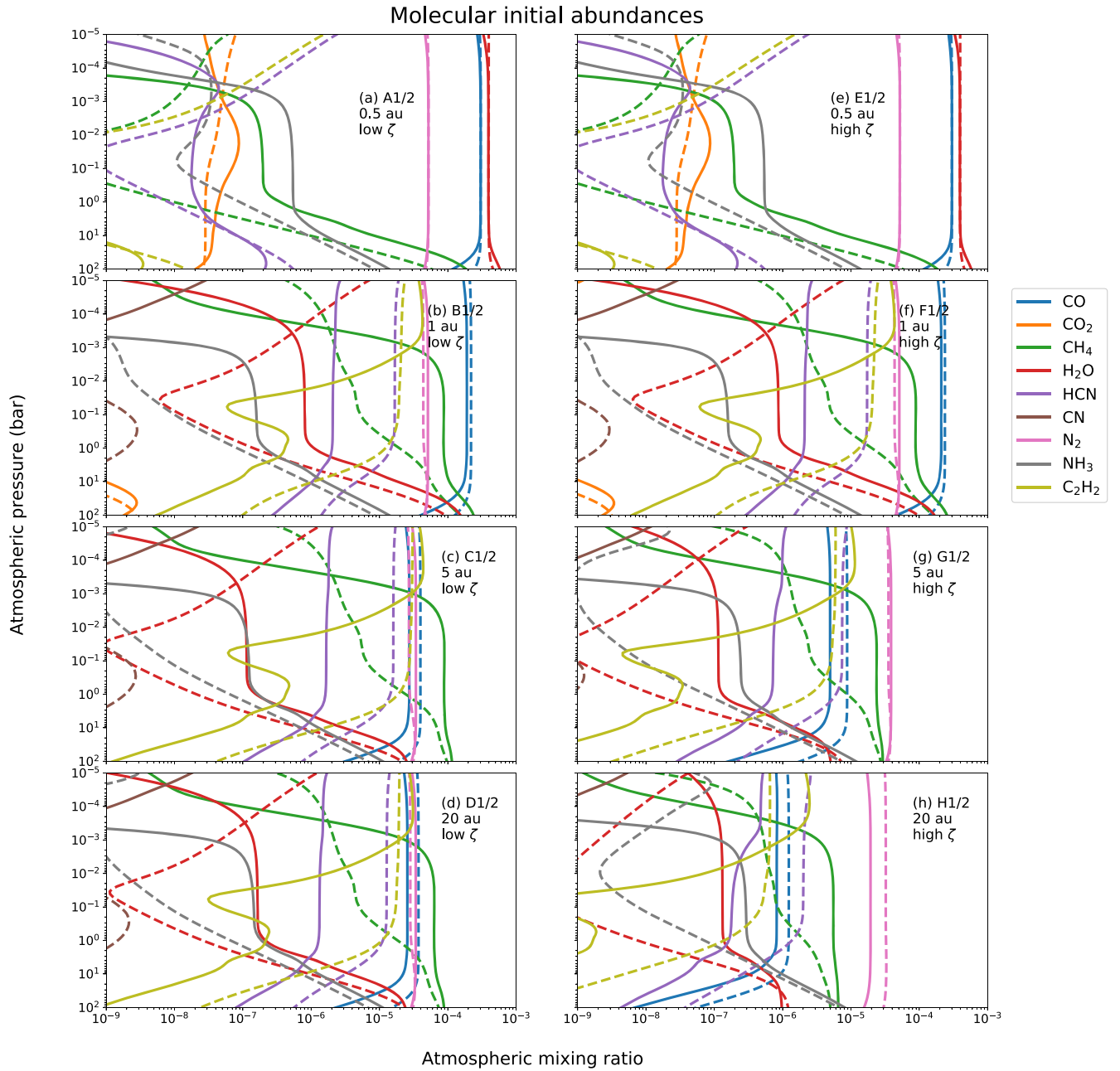**Figure 3.** Mixing ratios for specific volatiles (CO, CO_2, CH_4, H_2O, N_2, HCN, NH_3, and C_2H_2) in the atmosphere for HD 209458b for different positions (0.5, 1, 5, and 20 au) of local gas accretion and varying levels of disk ionization (ζ) in the case of molecular initial abundances (inheritance scenario). Solid lines are for an inverted *P–T* profile, and dotted lines are for a noninverted *P–T* profile. Chemical evolution is assumed to happen at the current location of the exoplanet.

CH_4–CH_3–C_2H_4–C_2H_3–C_2H_2 for low C/O ratios (A1) or CH_4–CH_3–C_2H_5–C_2H_4–C_2H_3–C_2H_2 for high C/O ratios (B1-D1; Figure 2).

N_2 and NH_3 are very insensitive to changes in all panels because they do not have any C or O, and the N/H values do not differ much for our input values, and also because both of them are significant carriers of N. However, while N_2 has a constant mixing ratio for almost all pressure levels, NH_3 shows a behavior of fall, quench, and fall for its profile similar to that of CH_4 because both NH_3 and CH_4 undergo kinetic conversion reactions to N_2 and CO, respectively (see Figure 2). N_2 and CO in turn are both major species in the atmosphere, and in our cases, they are quenched for most of the atmosphere. In addition, NH_3 is an essential molecule for producing HCN in

all models using the NH_3–HCN pathway. Thus, NH_3 is still indirectly but weakly dependent on the C/O ratio. This behavior for all species discussed until now is expected and is seen in other disequilibrium models (Moses et al. 2011; Venot et al. 2012; Hobbs et al. 2019) for this planet.

The mixing ratio of HCN gradually rises with increasing C/O ratio because the amount of carbon available for reactions with nitrogen increases and is highest at B1-D1. The behavior of HCN is more complex than that of the other species we have considered, however, and is determined by the quench and equilibrium levels of NH_3, CH_4, and H_2, as seen in the profile discussions for CH_4 and NH_3 above. Apart from A1, where HCN never finds a quench level because its production is too inefficient, B1-D1, with high C/O ratios, have enough C

(through CH_3) for HCN production to be fast, resulting in high enough abundances to be quenched upward of 1 bar.

The mixing ratio of C_2H_2 is overall pretty low in the lower atmosphere in all panels, but it becomes prominent for the mid-atmosphere and upper atmosphere as the C/O ratio is increased. For low C/O ratios (A1), C_2H_2 is produced by CH_4–CH_3–C_2H_4–C_2H_3–C_2H_2, where the CH_3–C_2H_4 step is a slow rate-limiting step mediated by the excited singlet $^1CH_2$. C_2H_2 reaches a stable mixing ratio value (but not an actual quench level) at around 1 mbar only for supersolar C/O ratios (B1-D1), where it proceeds by the pathway CH_4–CH_3–C_2H_5–C_2H_4–C_2H_3–C_2H_2. The rate-limiting step is the formation of C_2H_5 by reaction of two CH_3 radicals. The abundance of CH_3 is increased high up in the atmosphere by the dissociation of CH_4. The rate of C_2H_5 formation is about three times faster in this model than in A1.

CO_2 also becomes more prominent only at lower C/O ratios where it can compete with CO, and overall, its abundance is very sensitive to the C/O ratio because O becomes a limiting element as C/O increases. CN, while included here, is not detected in the lower atmosphere in any of the plots, but does appear in the atmosphere above 0.1 mbar for supersolar C/O ratios as dissociation of HCN becomes viable. This sensitivity of CH_4, HCN, C_2H_2, and CO_2 to the C/O ratio is already expected from results of disequilibrium chemical kinetics (Moses 2014).

For the case of molecular initial abundances with high ionization with a temperature inversion shown in panels (e), (f), (g), and (h) in Figure 3 (solid lines), corresponding to models E1 to H1, the dominant volatile (apart from H_2 and He) depends on the assembly location in a similar way to the low-ionization case. For E1, the atmosphere is dominated by H_2O (due to the subsolar C/O ratio at this location), for F1, it is CO, and for G1 and H1, the main molecule is N_2. The difference in the main volatile between C1-D1 compared to G1-H1 is due to an overall depletion in absolute abundance of C/H by about a magnitude for the high-ionization cases. In comparison, the N/H abundances for the high-ionization cases remain almost the same as with the low-ionization cases—this is illustrated by the reduced C/N ratios in Table 1.

The mixing ratio for CH_4 steadily increases with the C/O ratio (as already explained above), and it becomes the second dominant volatile in F1, G1, and H1. N_2 and NH_3 remain insensitive to changes in all panels as absolute N/H abundances do not change much. In general, the mixing ratio profile behavior for models E1 and F1 are the same as their low-ionization counterparts (models A1 and B1), but models G1 and H1 differ from what we might expect based on their low-ionization counterpart (model D1, based on the C/O ratio). Model G1 has a slightly lower C/O ratio than D1, but with much lower initial absolute C/H and O/H abundances, which causes the overall shift of all profiles with C and O to the left. Even though D1 and H1 have the same C/O ratios, the effect of increased cosmic-ray ionization on chemistry is very clear, as the mixing ratios of all C- and O-bearing species are much lower in H1 than in D1. This is because the initial abundance of both C/H and O/H is an order of magnitude lower for H1 (the values are even lower than the level for G1) than for D1. HCN in H1 has a more complicated behavior, with two quench levels instead of the one seen in C1 and D1. One quench level is at the location of the CO-NH_3 quench level (in the lower atmosphere at around 1 bar) and the other is at the location where both CH_4

and NH_3 abundances start to fall (in the upper atmosphere at around 1 mbar). The absolute C/H depletion might be the cause of this profile behavior as well, considering that the reaction pathway is the same as in previous cases.

For the case of molecular initial abundances with low ionization and no temperature inversion shown in panels (a), (b), (c), and (d) in Figure 3 (dotted lines for a noninverted P–T profile) corresponding to models A2 to D2, the dominant volatile (apart from H_2 and He) goes from H_2O (subsolar C/O ratios) in A2 to (mostly) CO in the rest of the three panels (supersolar C/O ratios). Unlike the case with a temperature inversion, CH_4 is never a prominent volatile in the mid-atmosphere and upper atmosphere as in the temperature inversion case, but does increase in mixing ratio level as C/O increases. The reason is that several other reaction pathways in the CO-CH_4 interconversion (see Figure 2) become possible in the lower and mid-atmosphere because the noninverted P–T profile is considerable hotter than the inverted P–T profile for much of the atmosphere below the 1 mbar level. However, above the 1 mbar level, the mixing ratio of CH_4 is higher than in the case of an inverted profile because the noninverted profile is now cooler than the inverted profile, which reduces the rate of its dissociation.

N_2 remains very insensitive to the C/O ratio as in all other cases. H_2O, and hence CO_2, on the other hand, remain very sensitive to C/O. However, the behavior of H_2O is different than in the inverted profile cases as its mixing ratio decreases more rapidly, but then increases just above the 0.1 bar level. This level coincides with the pressure level above which the inverted P–T profile starts exhibiting its inversion by heating up, while the noninverted profile continues to cool down. So, while the dissociation of water becomes enhanced for the inverted profile (even more after it cools down from 1900 K), the formation reaction rates are enhanced for the noninverted profile going below that temperature, resulting in the profile difference seen here.

NH_3 is less prominent than in cases without a temperature inversion as most of it either quickly reacts with CH_3 (from CH_4) for B2-D2 (high C/O ratio) to form HCN through the same NH_3–HCN pathway mentioned before. The kinetic interconversion of NH_3 and N_2 is also not fast enough for NH_3 to reach a quenching level because the rate-limiting steps (N_2-N and N_2H-N_2H_2) of the two responsible chemical pathways (see Figure 2) are very slow.

HCN quenches at higher mixing ratios at the same pressure levels as in the cases with a temperature inversion for B2-D2. In A2, HCN becomes very prominent in the upper atmosphere. This is because HCN, in addition to being the product of faster NH_3–HCN and CH_4–HCN pathways mentioned before, is also a main step in all three CH_4–C_2H_2 pathways that are possible in these cases. The conversion from HCN into HC_3N (followed by a conversion into C_2H_2) mediated by ^1C_2H is a rate-limiting step in all these pathways. Since C_2H_2 is correlated with HCN, the mixing ratio profiles for both molecules behave similarly in all models. In addition, C_2H_2 is also formed by one pathway in the CH_4–CO interconversion process. So, the level of C_2H_2 is sometimes slightly higher than the level of HCN in mid and upper atmospheres. However, HCN is more spectrally significant due to its higher opacity, which often overshadows that of C_2H_2 in the corresponding transmission spectrum plots.

For the case of molecular initial abundances with high ionization and no temperature inversion shown in panels (e),
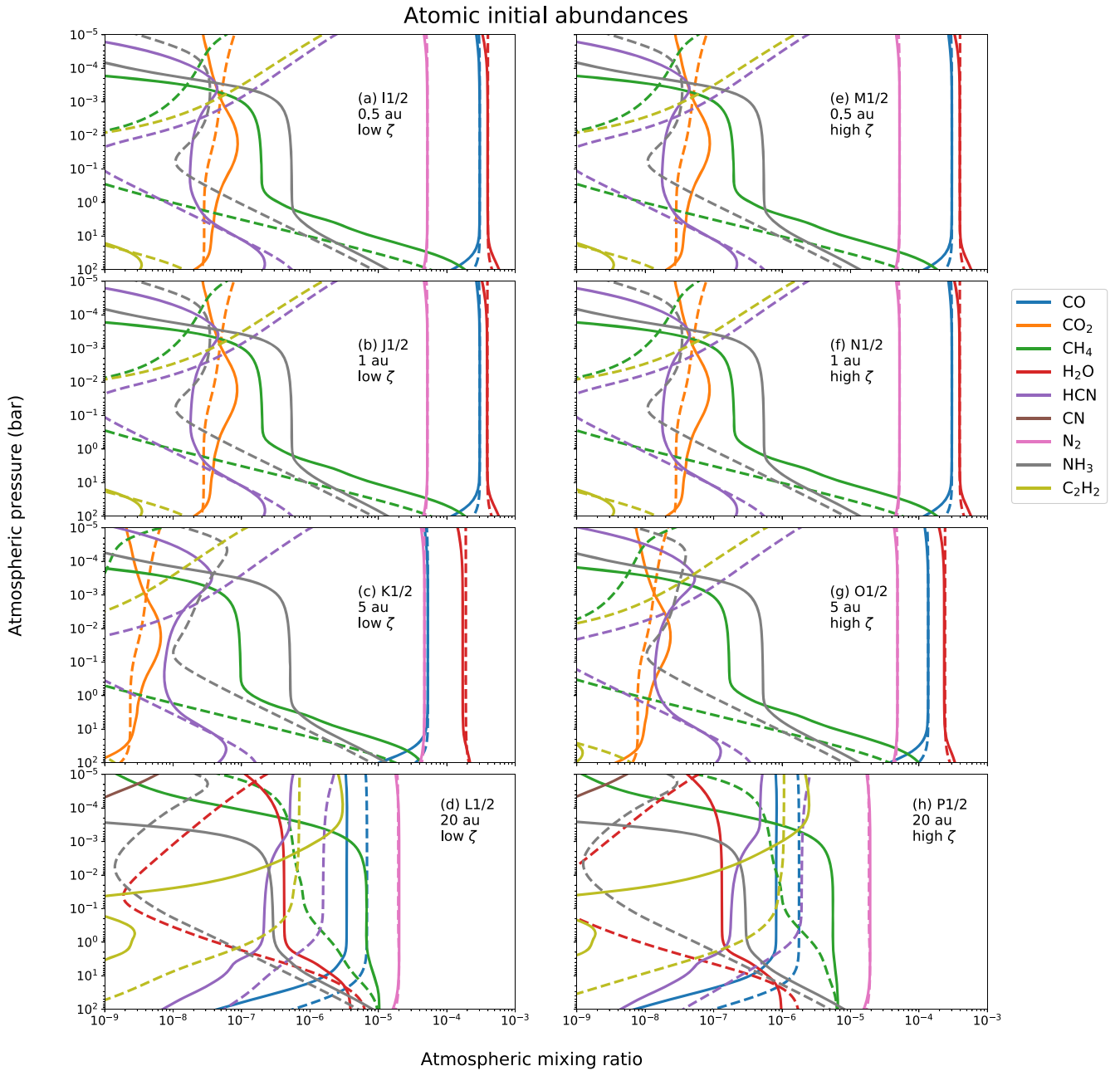
Atomic initial abundances

Figure 4. Mixing ratios for specific volatiles (CO, CO_2, CH_4, H_2O, N_2, HCN, NH_3, and C_2H_2) in the atmosphere for HD 209458b for different positions (0.5, 1, 5, and 20 au) of local gas accretion and varying levels of disk ionization (ζ) in the case of atomic initial abundances (reset scenario). Solid lines are for an inverted P–T profile, and dotted lines are for a noninverted P–T profile. Chemical evolution is assumed to happen at the current location of the exoplanet.

(f), (g), and (h) in Figure 3 (dotted lines) corresponding to models E2 to H2, the behavior of the main volatiles is the same as in the case of low ionization. Models E2 and F2 have a similar behavior as A2 and B2, which have similar C/O ratios. However, H2 does not have a similar profile behavior as D2, even though both have similar C/O ratios, because its C/H and O/H are more than an order of magnitude lower than in D2. This causes almost all of the mixing ratio profiles to shift to the left.

The difference in the solid mixing ratio profiles between G1 and H1 with respect to D1 and between the dotted mixing ratio profiles H2 with respect to D2 for Figure 3 shows that it is not just the C/O ratio of the gas, but also the overall absolute abundances that affect the chemistry in atmospheres. This

absolute abundance value is set by the level of chemical processing in the disk. This overall abundance, however, is reflected in changes in both C/O and C/N ratios together, as seen in Table 1. Hence, both the C/O and C/N ratios taken together can provide a more accurate description. This was the basis for Notsu et al. (2020) and Turrini et al. (2021), who used the O/H ratio in addition to the C/O ratio, and the C/O and C/N ratios together, respectively, to comment on formation locations.

3.1.2. For Atomic Initial Abundances

For the case of atomic initial abundances with low ionization with a temperature inversion shown in panels (a), (b), (c), and (d) (solid lines) in Figure 4 corresponding to models I1 to L1,

H_2O and CO are the main volatiles (apart from H_2 and He) in the atmosphere for I1-K1 (subsolar C/O ratios), whereas N_2 is the dominant volatile for L1. Even though the C/O for L1 is closer to I1 and J1, the overall initial C and O abundances with respect to H are about an order of magnitude lower, while N/H mostly remains the same, and this is reflected in the C/N ratios. The depletion causes mixing ratio profiles in L1 to behave like models with high C/O ratios (for a thermally inverted profile). This is also reflected in the reaction pathways, with the one for CH_4–C_2H_2 being the same as in high C/O models with a thermally inverted profile. Other than the anomalous behavior of L1, all other models behave as expected based on their C/O ratios, as mentioned in the cases before.

Models with atomic initial abundances, high ionization, and a temperature inversion are shown in panels (e), (f), (g), and (h) in Figure 4 (solid lines), corresponding to models M1 to P1. H_2O and CO (apart from H_2 and He) are again the dominant volatiles in most cases (subsolar CO ratios), except for P1, which has supersolar C/O, and where N_2 and CH_4 are dominant. N_2 and NH_3 continue to be insensitive for the same reasons as pointed out before. All models behave as expected based on their C/O ratios.

For the case of atomic initial abundances with low ionization with no temperature inversion shown in panels (a), (b), (c), and (d) in Figure 4 (dotted lines), corresponding to models I2 to L2, H_2O (apart from H_2O and He) is the predominant volatile (subsolar C/O ratios), followed by CO, except for L2, where N_2 is the dominant volatile, followed by CO. All models except for L2 behave as expected based on their C/O ratios. However, the chemical pathways for these models do sometimes differ from their molecular abundance counterparts. The case for L2 as an anomalous case was also made in the case of a thermally inverted profile (model L1). So, the abundances used for these models (L1/2) can cause the transmission or emission spectrum to behave as one for a high C/O ratio, even though the actual C/O ratio would be subsolar.

For the case of atomic initial abundances with high ionization with no temperature inversion shown in panels (e), (f), (g), and (h) in Figure 4 (dotted lines), corresponding to models M2 to P2, H_2O (apart from H_2 and He) is almost always dominant, with CO following it (subsolar C/O ratios), except for P2, which has a supersolar C/O ratio and behaves similar to L2 and other models with high C/O ratios. All models behave as expected based on their C/O ratios.

3.2. Synthetic Transmission and Emission Spectra

3.2.1. Transmission Spectra

The transmission spectra are shown in Figure 5 for cases with a temperature inversion (models A1 to P1) and in Figure 6 for cases without a temperature inversion (models A2 to P2). The absorption spectral features of H_2O, CO, CO_2, HCN, CN, CH_4, C_2H_2, and NH_3 are summarized in Table 2. Accordingly, all panels in Figures 5 and 6 can be divided into three types of spectra: majority H_2O, majority CH_4, and majority CN-HCN.

Figure 5(a) shows the spectra generated for models with a temperature inversion, low ionization, and molecular initial abundances (models A1 to D1). The molecules that generally dominate the spectra correspond to those with high abundances in the models in Figure 3. B1, C1, and D1 have very similar spectra, with prominent CH_4 (mixed with low HCN, H_2O, and NH_3) signatures in the 1–10 μm range, followed by a small

NH_3 peak at 10 μm, followed by a significant HCN+C_2H_2 peak at 13–14 μm, and ending with an almost flat spectrum from 15–25 μm due to the presence of HCN, NH_3, and H_2O. There is also a small peak at 4.1 μm corresponding to CO. For A1, the predicted spectrum is almost entirely due to H_2O, which dominates all other features in the 0.6–25 μm range. The concave 10–25 μm spectrum, while being shaped by H_2O, also has contributions from NH_3 and CO_2. A1 also has a small broad peak at 4–4.1 μm due to the presence of both CO_2 and CO. All the models show prominent CN features at 0.3 μm, however. Considering that CN is not very abundant in the atmospheres in these models, this is made possible by the high opacity of CN at these wavelengths.

In Figure 5(b) we can see that models E1 to H1 (similar to models A1 to D1, but with high ionization instead) result in similar spectral features as the previous models, and these can also be explained using the same logic as above. Hence, for the complete case of molecular initial abundances with thermal inversion, a supersolar C/O ratio with HCN, CH_4, H_2O, CO, CN, and NH_3 signatures would indicate gas accretion anywhere between 1–20 au, i.e., between the H_2O and CO ice lines, but a H_2O predominant spectrum, with CO_2 and CO detection at 4–4.1 μm, would point to accretion interior to the H_2O ice line and a C/O ratio lower than solar.

For models I1 to L1 and M1 to P1 (atomic initial abundances with temperature inversion, and low and high ionization), the situation is completely flipped, with H_2O predominated spectra dominating the cases (Figures 5(c) and (d)). The only models in these sets that are not dominated by H_2O features are for accretion at 20 au (models L1 and P1), i.e., between the CH_4 and CO ice lines. Models L1 and P1 both show features comparable to B1-D1, as mentioned above, but with reduced width and height of the secondary features due to depleted overall abundances that leave the CH_4 features more prominent between 1–10 μm. For L1, this is anomalous as it has a subsolar C/O ratio. In the case of atomic initial abundances with thermal inversion, H_2O-dominated spectra with CO_2 and CO detection at 4–4.1 μm would therefore point to gas accretion interior to the CH_4 ice line for subsolar C/O ratios in both types of ionization conditions. However, a spectrum dominated by CH_4 that also includes an HCN+C_2H_2 signature at 13–14 μm can indicate accretion between the CH_4 and CO ice lines for a subsolar C/O ratio and low ionization and supersolar C/O with high ionization.

For atmospheres with molecular initial abundances and without a thermal inversion (models A2 to H2), all of the predicted spectra can be grouped into either H_2O dominant or HCN(+CN) dominant (Figures 6(a) and (b)). While H_2O completely dominates A2 and E2, there are also small features of CO_2 at 4 μm and contributions from NH_3, CO_2, HCN, and C_2H_2 in the flat spectrum after 10 μm. This is in line with the chemistry of these models, as shown in Figure 3. For B2-D2 and F2-H2, HCN has prominent features starting from around 1.1 μm. There are CO, CH_4 and C_2H_2 features mixed in there as well. However, the CN features are now very prominent and are detected in the 0.3–1.1 μm range. In addition, the HCN-C_2H_2 peak at 13–14 μm is even more prominent, followed by a dip until 25 μm, with contributions from H_2O and NH_3 as well. Hence, in the case of molecular abundances without a thermal inversion, a predominant H_2O spectrum would indicate accretion within the H_2O ice line, but an HCN
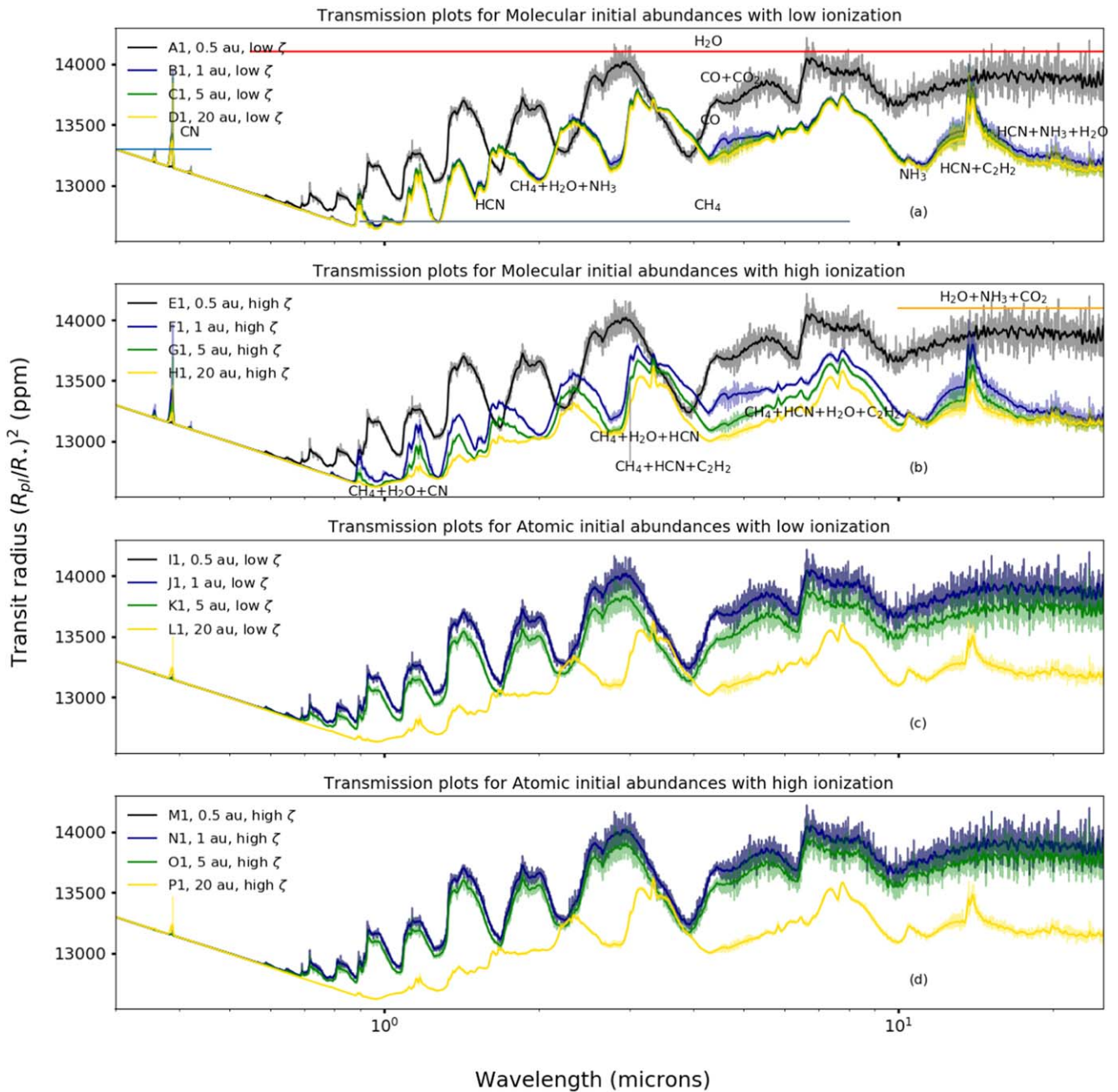
Figure 5. Synthetic transmission spectra for all cases of abundances considered for chemistry in the atmosphere of HD 209458b with thermal inversion. The peaks for H_2O and CH_4 are multiple and span the entirety of red and gray horizontal lines (the signature of any other species falling in between is specifically labeled). The faded spectra at the back have $R = 1000$, while the highlighted spectra for easy visibility are lower-resolution spectra obtained by convolving the original spectra with a Gaussian kernel with a standard deviation of 3, following the prescription suggested in Zilinskas et al. (2020).

(+CN)-dominated spectrum would indicate accretion within the CO_2 and CO ice lines for both types of possible ionizations.

For models I2 to P2 (the case of atomic initial abundances for a noninverted P–T profile (panels c and d of Figure 6), H_2O dominates almost all the spectra, as is expected based on the chemistry for these particular models (Figure 4). Hence, H_2O would be the dominant spectral signature for gas accretion interior to the CH_4 ice line for all such cases. For gas accretion within the CH_4 and CO ice lines, the spectrum has a similar behavior to B2-D2 or E2-H2. The anomalous case for L2 being subsolar but showing supersolar features is similar to L1. Hence, in the case of atomic abundances without a thermal

inversion, a predominant H_2O spectrum would indicate accretion within the CH_4 ice line, but a HCN(+CN)-dominated spectrum would indicate accretion within the CH_4 and CO ice lines.

3.2.2. Emission Spectra

The emission spectra for all models with a thermally inverted profile (models A1 to P1) are shown in Figure 7 and for a P–T profile without inversion (models A2 to P2) in Figure 8. The molecular signatures in both these sets of spectra are noticeably harder to discern from those in the transmission spectrum plots,
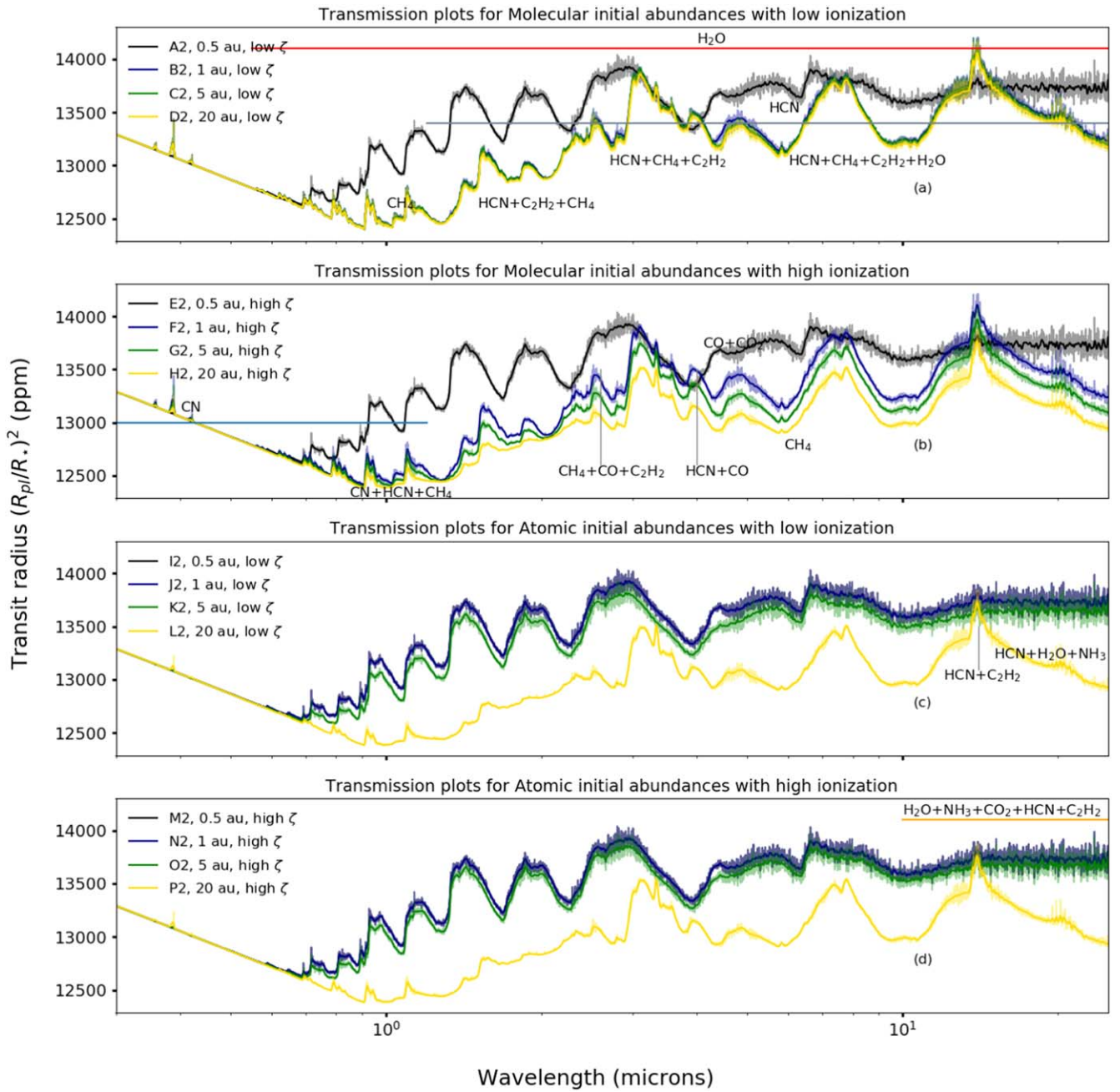
Figure 6. Same as Figure 5, but for a *P–T* profile without thermal inversion. In addition, CN peaks span the horizontal blue line.

Table 2
Features Exhibited by a Few Spectrally Significant Molecules

Molecule	Spectral features (μm)
H_2O	0.7–0.8, 0.8–0.9, 1, 3 peaks between 1–2, 2–4, 5, broad features at 7–9 and 10 onward
CH_4	0.9, 1, 3 peaks between 1–2, 2.5, 3.5 and broad feature from 6–9
NH_3	2–3 feature, 10 and broad feature from 10–25
CO and CO_2	4.1 and 4, 14
HCN	1.4, 1.5, 1.8, 2.6, 2.9, 3.1, 3.6, 4, 5, 7–9, 10, 13 and 20
CN	0.3–0.5 and 0.7–1.1 (sharp jagged peaks)
C_2H_2	features from 1.5–2, 3–4, 7–9, peak at 14
H_2 and He Rayleigh scattering	Negative slope from 0.3–1.2

which means that observationally, it might be preferable to focus on obtaining primary or transit spectra for this planet.

In Figure 7, the most prominent feature for A1, E1, J1-K1, and M1-O1 are the broad water features at 3–4 μm, 4–7 μm, and 7–9 μm. In addition, the small peak for NH_3 at 10 μm can also be slightly differentiated. For B1-D1, F1-H1, L1, and P1, the features that are more difficult to differentiate include the slight kinks between 3–4 μm, 4–5 μm, and 8 μm for CH_4. This type of mostly featureless emission spectra were also seen in Drummond et al. (2016) using a *P–T* profile with thermal inversion for non-equilibrium chemistry (ATMO code) in HD 209458b.

The emission spectra for all abundance values with a profile that is not thermally inverted are shown in Figure 8. It can be seen that all these plots have more well-defined spectral features than the case with thermal inversion. The absorption features for
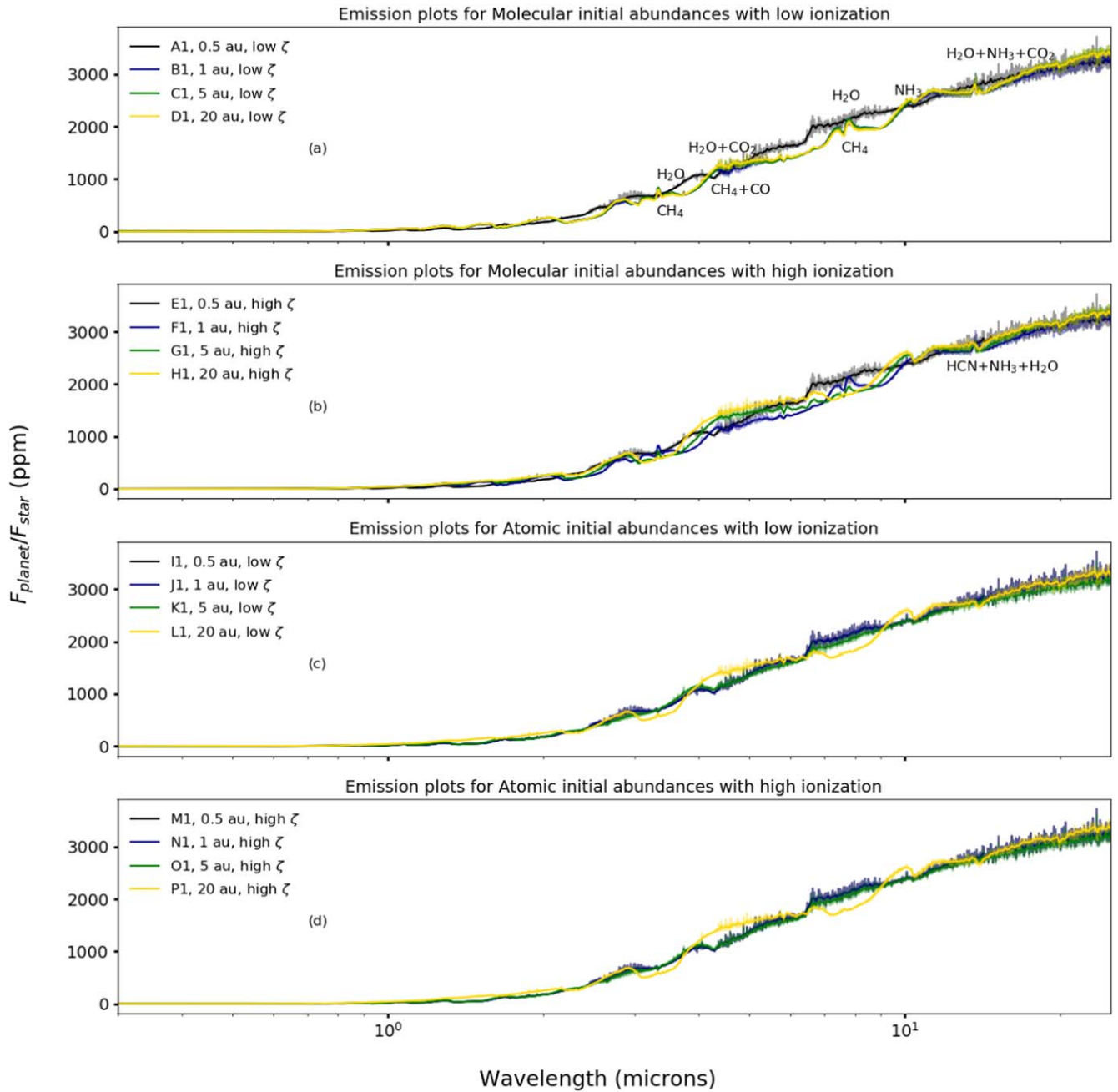
Figure 7. Synthetic emission spectra for all cases of abundances considered for chemistry in the atmosphere of HD 209458b with a P–T profile with thermal inversion. The broad peaks for H_2O at 7–9 μm and NH_3 at 10 μm alone can be reasonably well discerned. The faded spectra at the back have a $R = 1000$, while the highlighted spectra for easy visibility are lower-resolution spectra obtained by convolving the original spectra with a Gaussian kernel with a standard deviation of 3.

HCN are now prominent for all cases with an HCN-dominated spectrum (B2-D2, F2-H2, L2, and P2), with multiple troughs ranging between 2.5–25 μm. For A2, E2, I2-K2, and M2-O2, the H_2O absorption features can also be seen. For all the plots, the conclusion remains the same as for the transmission spectra.

4. Discussion

4.1. Comparison with Equilibrium Plots Using TEA

Our parameters for non inverted P–T profile plots for HD 209458b roughly coincide with the parameters for a hot Jupiter accreting gas from the disk with differing initial abundances depending on the position in the disk (as we have also considered) and migrating to 0.05 au in Notsu et al. (2020),

where it evolves its atmospheric chemistry. However, Notsu et al. (2020) used an analytical P–T profile obtained from Guillot (2010). Thus, it is possible to compare the effects of disequilibrium over equilibrium as well as any difference resulting from the variations in the P–T profiles on the chemistry of these atmospheres. We henceforth compare the dotted mixing ratio profiles in Figures 3 and 4 to the left plots of Figures 3, 4, 5, and 6 in their paper.

The most prominent difference in all plots is in the behavior of HCN. VULCAN disequilibrium chemical kinetics predicts more HCN in the atmosphere than the TEA equilibrium plots in all model cases. The level of HCN predicted by TEA would lead to an underprediction of HCN in both the emission and transmission spectra. Hence, the presence and level of HCN in
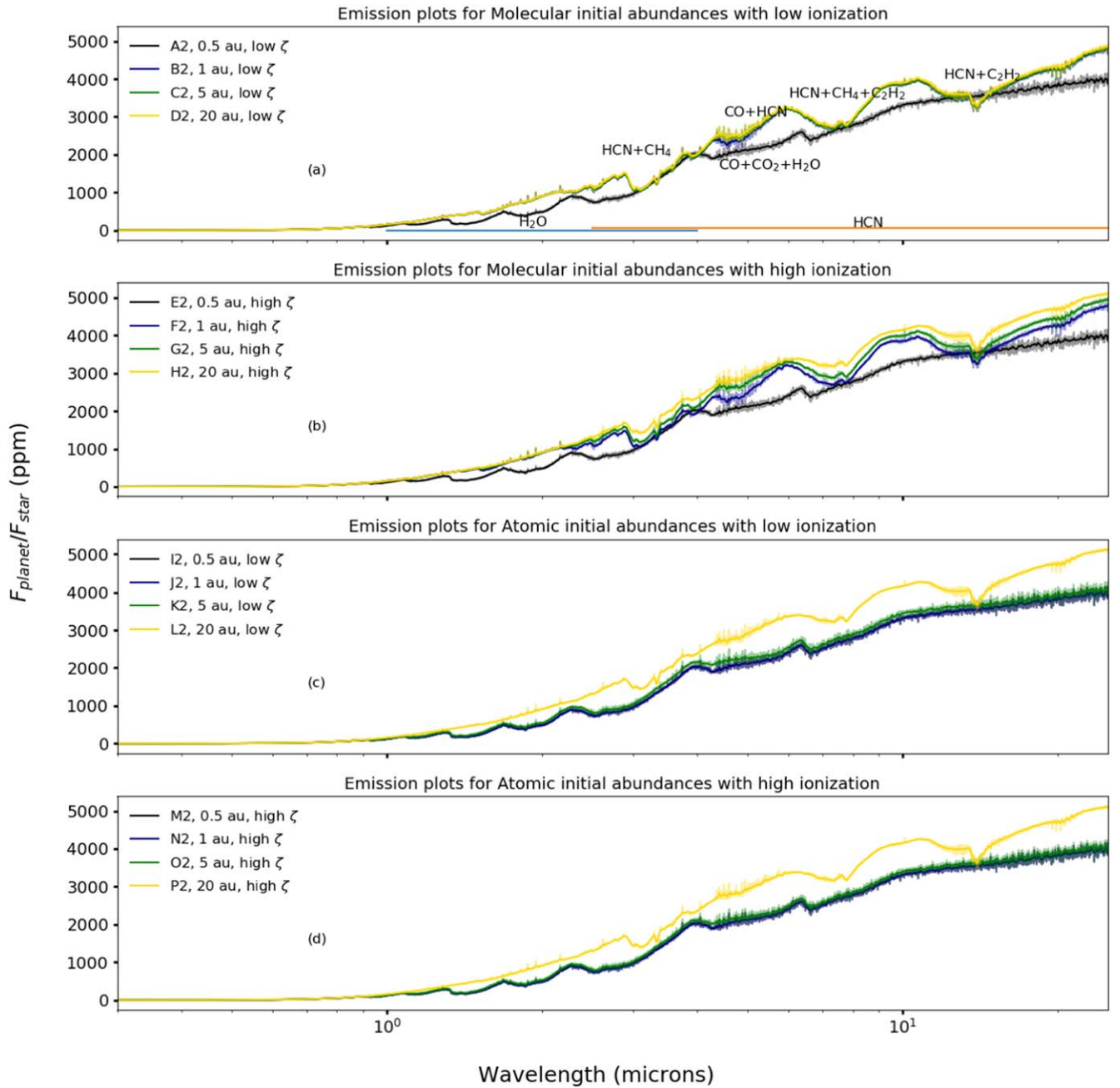
Figure 8. Same as Figure 7, but for a P–T profile without thermal inversion.

observed spectra for HD 209458b would be a good predictor of whether the atmospheric chemistry in the atmosphere is in disequilibrium. This is an expected outcome because HCN is a byproduct of reactions and quenching levels between CH_4-NH_3 and CO-NH_3 and the level of H_2 and is expected to be detected at larger abundances in hot Jupiters as a notable departure from chemical equilibrium calculations (Moses et al. 2011; Moses 2014). This study validates it for HD 209458b and shows the importance of using disequilibrium chemistry calculations over equilibrium chemistry in a way where it can significantly affect spectral observations. In this way, it remedies one of the limitations of Notsu et al. (2020) that was already outlined in their work.

As also expected, C_2H_2 also shows more prominence in disequilibrium chemistry. The level is not enough for it to have a unique spectral fingerprint, however, as it is often overshadowed by the higher opacity of HCN in the same regions. Another difference is the overprediction of H_2O in the lower exoplanet atmosphere, but the underprediction in the upper atmosphere by TEA. This can change the shape of the transmission and emission spectra by changing the overall absorption due to H_2O in the regions of the atmosphere that are probed. The level of CH_4 and NH_3 is also greater in disequilibrium plots for most cases. This also means that their signatures can now be more prominent in the spectral plots.
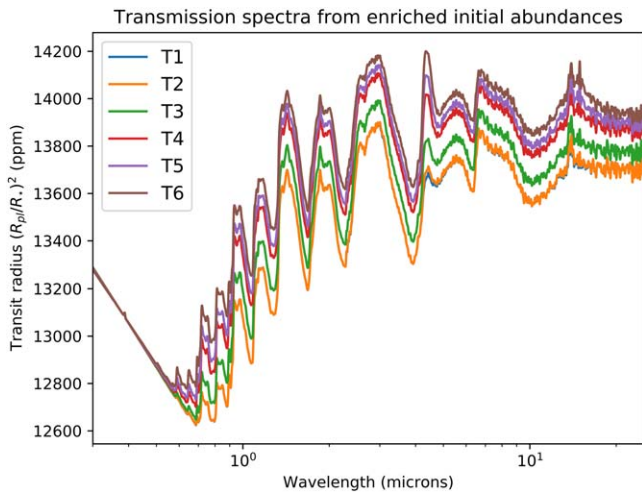
Figure 9. Effect on transmission spectra due to enrichment by solids. Initial elemental abundances are taken from Turrini et al. (2021), and the model labels are the same as in Table 1.

4.2. Examining the Presence of Thermal Inversion in the Atmosphere of HD 209458b

Both our chemistry and spectral results suggest that CH_4 is dominant for atmospheric chemistry using a thermally inverted profile at supersolar C/O ratios. Consequently, all cases of transmission spectra using such a profile show a major fingerprint of CH_4. However, a thermally noninverted profile still shows fingerprints of CH_4, but overall, it is dominated by HCN in both the transmission and emission spectra. Thus, a major presence of CH_4 in an obtained transmission or emission spectrum for HD 209458b could be a good indicator of whether the temperature profile in the atmosphere is inverted, similar to Moses et al. (2011), or noninverted, similar to the P–T profile used here. Either case would be a good indicator of supersolar C/O ratios.

However, it must be noted that a CH_4 detection would only show a difference between the two specific profiles we have considered in this case study. Hence, this claim must not be used as a general fingerprint indicative of a temperature inversion in a hot Jupiter.

4.3. Limitations of This Work

The first limitation of this work is the limited chemical network used, which is a feature of VULCAN. Apart from this, we did not include sulfur chemistry in this work either. However, effects of sulfur chemistry using VULCAN have been discussed in Tsai et al. (2021). Hobbs et al. (2021a) recently showed that for the thermally inverted case for HD 209458b, inclusion of sulfur chemistry can reduce the abundance of species such as CH_4, NH_3, and HCN by about two orders of magnitude in between 10^{-3}–10^{-5} bar. This might dampen the corresponding spectral features in our spectra. The effect of clouds or aerosols was not considered in this work either. Both of these can also heavily affect the results of this work by damping most of the spectral features as well. Hence, the results of this study must strictly be seen in the case of cloud-free hot-Jupiter atmospheres alone.

Two other limitations from the chemical kinetics model itself are that VULCAN is a 1D model and is not self-consistent. While the P–T-Kzz profiles obtained from Moses et al. (2011) and HELIOS are definite upgrades compared to using just a

simple analytical P–T model based on Guillot (2010; used for all cases in Notsu et al. 2020), they still do not take into account the coupling between P–T profiles and the atmospheric chemistry evolution. In addition, 1D models assume a spherically symmetric case for the atmosphere and hence have a reduced computational cost. These simplifications neglect the more complicated 3D behavior of heterogeneous exoplanet atmospheres, however, which can affect the abundance of elements in the atmosphere and affect the overall analysis of this paper.

Limitations of the disk chemistry model used in this analysis arise from the fact that it follows the chemical evolution for a static protoplanetary disk within 1 Myr. Eistrup et al. (2018) looked at the evolution of abundances in an evolving disk until 7 Myr and found that consideration of the disk evolution is quite necessary and complicates the case of linking exoplanetary atmospheric markers to formation locations by changing significantly both the gas and solid C/O ratios over time. Disk masses are also hypothesized to be much higher within one million years (Manara et al. 2018; Appelgren et al. 2020; Dash & Miguel 2020; Miguel et al. 2020), and hence even with the timescale used in this static model, significant disk evolution could have occurred, which makes the case of a static disk assumption suspect.

In our work, we also did not consider the case of contamination by solids. However, this contamination can greatly change the results by changing the effective C/O ratio of the envelope. In the case of a static disk, looking at the effect of contamination from disk solids can be gauged by whether the solid C/O ratios are overall greater or lower than the gas C/O ratios. For the case of molecular abundances, Eistrup et al. (2016) showed that the solid C/O ratios are always lower (with an upper limit of 0.4) than the gas C/O ratios. Hence, contamination would lead to a decrease in atmospheric C/O ratios and give us a location in the disk far more in compared to where it should actually be. Turrini et al. (2021) used this specific case of molecular initial abundances to look at the effect of C/O ratios due to the enhancement from solids accreted from the disk. We use their initial C/H, O/H, and N/H abundances (see Table 1) to recalculate the atmospheric chemistry calculations (using our noninverted P–T profile), and the resultant plot is shown in Figure 9. All the plots show H_2O-dominated features because the resultant atmospheric C/O ratios are now closer to a value of about 0.5, which is subsolar. The one absorption feature that prominently grows with distance is the CO_2 feature at 4–4.1 μm. The HCN and CO_2 peaks (at 13–14 μm) also start bifurcating and become more prominent with increasing distances.

From Eistrup et al. (2016), we can also glean that for the case of atomic initial abundances, the solid C/O ratios at locations >2 au are higher (with an upper limit of 0.55) than the gas C/O ratio. Contamination here would hence have the opposite effect and give us a location much farther out than where it should actually be. In the evolving-disk scenario of Eistrup et al. (2018), this situation is even more complex as gas C/O ratios can evolve and become lower than the evolved solid C/O ratios even in the case of molecular initial abundances. While considering these cases to test our model-dependent results is beyond the scope for this study, they can be the subject of future research work.

Yet another limitation is that the other mode of giant planet formation—disk fragmentation from gravitational instability is

also neglected by this model. Hobbs et al. (2021b) recently reported a similar analysis for this formation mechanism and found that such a model within the CO and CO_2 ice lines can also explain the formation mechanism of HD 209458b.

Other limitations of this work include the assumption of an initial global C/O of 0.34 for the disk chemistry calculation and the assumption that rapid gas accretion can occur in a limited region close to the disk midplane. The validity of all these has been described in detail in Notsu et al. (2020). Our work is intended to serve as an extension to their work and hence inherits many of the same limitations of the original work.

4.4. Accretion Location from Spectral Observations

Although validation of the list of species in the atmosphere of HD 209458b is still not very complete, nevertheless the detection of H_2O, CH_4, CO, NH_3, and HCN presents an opportunity to understand at which disk location HD 209458b could have accreted most of its envelope.

From all the different transmission spectra we have constructed by varying the initial gas elemental abundances based on disk location from Notsu et al. (2020), we can exclude all majority H_2O spectra, i.e., A1/A2, E1/E2, I1/I2-K1/K2, and M1/M2-O1/O2 because they show the spectral fingerprints of only NH_3, CO, and CO_2 other than H_2O. The only transmission spectra that allow for the presence of all of H_2O, CH_4, CO, NH_3, and HCN are B1/B2-D1/D2, F1/F2-H1/H2, L1/L2, and P1/P2. Except for L1/L2 (C/O of 0.41), all other cases have supersolar C/O ratios. These point to a gas accretion location outside the H_2O ice line, and more specifically, between the CO_2 and CO ice lines for molecular initial abundance cases and between the CH_4 and CO ice lines for the atomic initial abundance cases. For the cases of an inverted P–T profile, the spectrum as a whole is characterized by majority CH_4 signatures, while for the case of a noninverted P–T profile, it is characterized by majority HCN signatures. In both cases, it is difficult to discriminate between the difference in chemical processing of the initial disk just based on the spectrum, and it would require the measurement of the abundances specifically by retrieval.

Our specific result of a supersolar C/O ratio and formation between the CO and CO_2 ice lines (for a core accretion formation mechanism) is in agreement with the findings of both Giacobbe et al. (2021) and Hobbs et al. (2021b), who found a formation location beyond the CO_2 ice line. Giacobbe et al. (2021) found a supersolar C/O ratio close to 1, and while they found the formation location to be beyond the H_2O ice line, they found a likely location between the CO_2 and CO ice lines. While Giacobbe et al. (2021) performed their analysis on the assumption of thermochemical equilibrium, the analysis of Hobbs et al. (2021b) and our analysis are based on disequilibrium chemistry from a range of initial abundances obtained from disk chemistry simulations. The lack of a difference might arise because HD 209458b is still a hot planet where thermochemical equilibrium largely dominates disequilibrium. For cooler planets, this might no longer be the case. The other specific result corresponding to L1/2 for subsolar C/O ratios and gas accretion between the CH_4 and CO ice lines, however, is new and only exists because of an anomalous behavior caused by significant C/H depletion in the gas accreted from the disk. However, from the discussion in the

section below, it is unlikely to be a candidate, but it is nonetheless quite interesting.

The results of Giacobbe et al. (2021) also allow us to streamline possible models slightly further. The abundances of molecules obtained from their analysis for HD 209458b falls mostly beyond the values used in Turrini et al. (2021), as can be found from the comparison made in Hobbs et al. (2021b; except for H_2O). Considering that their initial abundances were protosolar or higher, only B1/B2 or F1/F2 are close enough to protosolar values to fall close to this range. These models would indicate gas accretion beyond the CO_2 ice line, but more specifically, between the CO_2 and CH_4 ice lines. Both models are molecular initial abundance cases and have supersolar C/O ratios. The rest of the model cases have depleted initial elemental abundances and would require enrichment from solids. As discussed in Section 4.3, enrichment using molecular initial abundance with low-ionization cases was used in Turrini et al. (2021), and the resultant spectra from Figure 9 shows that HCN, CO, and CO_2 start to become detected from T3-T6. This indicates formation beyond 19 au (i.e., beyond the CO_2 ice line, which is at 10.5 au for the disk model of Turrini et al. 2021), with an enrichment of the accreted envelope by disk solids while the core is migrating. In Section 4.3, we also discussed that atomic initial abundances and the case of evolving disks will complicate things even further. Looking at these cases is beyond the scope of this work, however.

4.5. Observability with the JWST

We now try to determine whether the three spectral cases (majority H_2O, majority CH_4, and majority HCN) that act as proxy for formation locations for this exoplanet can be differentiated using JWST observations. We have described the methodology of simulating such observations in Section 2.4. Since both B1/B2 and F1/F2 have very similar C/O ratios, initial gas-phase chemical abundances, and similar spectral plots, we just simulate the observation for the cases of B1 and B2. We also plot T1, T3, and T6 to determine whether they can be differentiated as well. We simulate only the transmission spectrs because it is clear from our work that they have more prominent features.

From Figure 10, it is easy to see that the important spectral features in our candidate spectra are indeed differentiable in transmission spectra. The CO_2 and CO peaks at 4–4.2 μm are very pronounced in the H_2O dominated spectra (A1, T1, T3, and T6). A1, T1, and T3 might be hard to distinguish overall, but T6 is distinguishable from the rest by the very prominent CO_2 feature. For the CH_4 dominated spectrum B1, the CH_4+HCN+H_2O+C_2H_2 broad peak from 5–9 μm is easily distinguishable from the other spectra. The narrow HCN+CO and the slightly broad HCN peaks at 4 and 5 μm are also easily detected. Likewise, for the HCN-dominated spectrum B2, it is easy to distinguish the dip at 6 μm and then the narrower peak due to HCN+CH_4+C_2H_2+H_2O until 9 μm. It is slightly difficult to detect the NH_3 peak at 10 μm for most spectra, however, especially in the H_2O dominated spectra. Overall, it seems likely that a simple inspection of the transmission spectra can provide ways to distinguish and observationally validate the potential linkage of the atmospheric composition of HD 209458b to its gas accretion location in the disk. This is summarized in a flowchart shown in Figure 11.
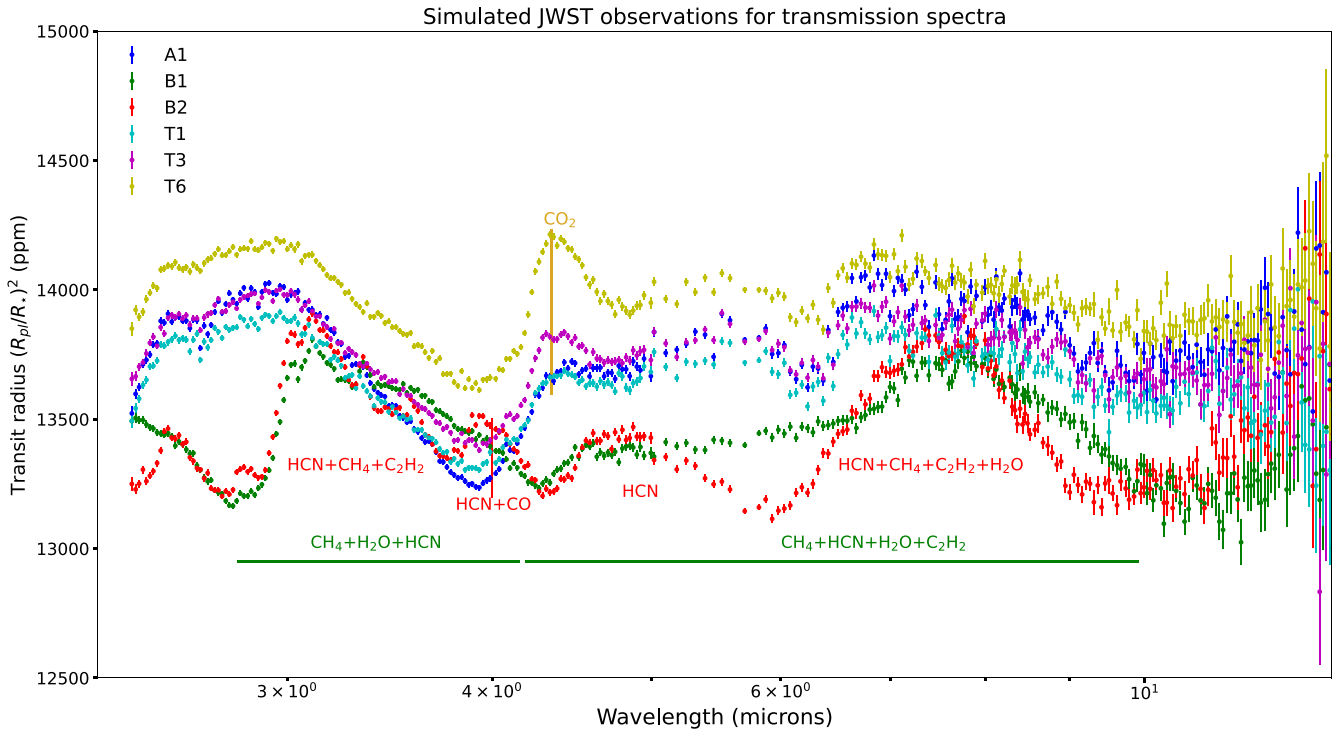
Figure 10. JWST simulated observations for transmission spectra for some selected models. A1, T1, T3, and T6 are H_2O-dominated spectra, but the increase in prominence of the CO_2 feature with increasing enrichment due to disk solid accretion is very clear, i.e., it increases from A1 (no enrichment—only disk gas contribution) to T6 (both disk gas and solid contribution). B1 is the CH_4-dominated spectrum, and specific molecular features are indicated in green. B2 is the HCN-dominated spectrum, and its associated features are indicated in red.
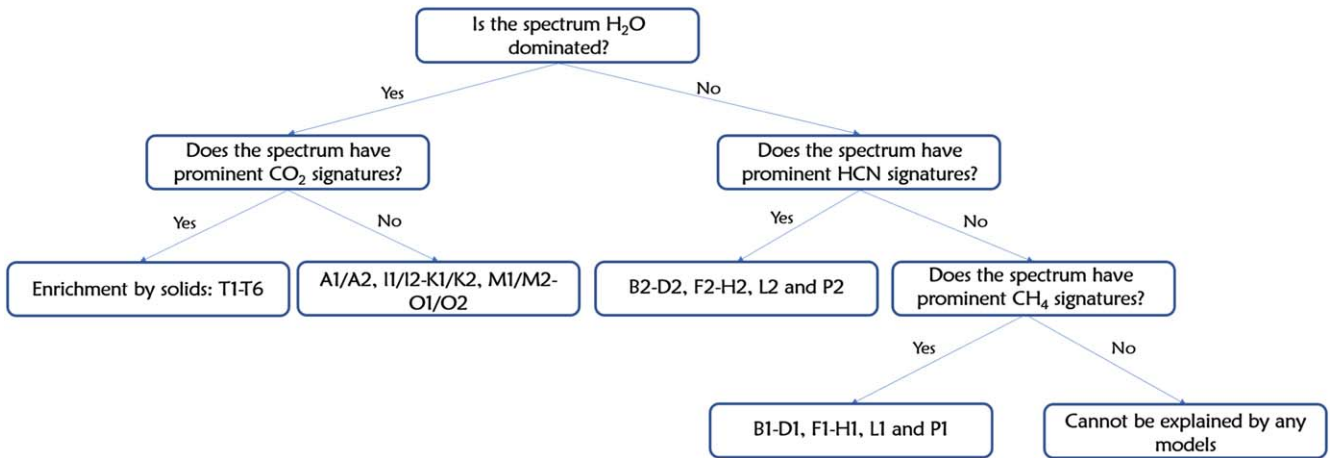
Figure 11. Flowchart showing the possible model scenarios with observational features that might be inferred using the JWST.

5. Conclusions

Chemistry in protostellar disks produces radial variations in the gas-phase abundances of elements including N, C, and O. In this work, we studied the specific case of the hot Jupiter HD 209458b and used the radially dependent abundances predicted by the disk chemical kinetics model of Eistrup et al. (2016) as initial abundances to predict its atmospheric chemistry. We evolved its atmospheric composition using a wrapper that coupled disequilibrium chemistry with a coupled chemical kinetics (VULCAN) radiative transfer (petitRADTRANS). We also considered the case of atmospheric evolution using two different P–T profiles: the thermally inverted profile used in Moses et al. (2011), and a thermally noninverted profile

constructed using the self-consistent radiative transfer code HELIOS (Malik et al. 2017).

We find that differences in initial abundances manifest in different mixing ratios of spectrally significant species in the atmosphere. HCN, C_2H_2, CH_4, and NH_3 are more abundant when vertical mixing, diffusion, and photochemistry are enabled to use disequilibrium chemistry, compared to equilibrium chemistry mixing ratios simulated using TEA in Notsu et al. (2020). Subsolar or supersolar C/O ratios (taken together with C/N ratios at times) are good indicators of relative abundances of molecules in the atmosphere if the absolute abundances of C/H and O/H are not very depleted, i.e., $>\sim 10^{-6}$. Depletion below this threshold can result in anomalous cases in which a subsolar C/O ratio can have

prominent HCN and C_2H_2 mixing ratios. Hence, the C/O ratio when combined with C/H or O/H or the C/N ratio indicates the location where most of the gas in the exoplanet envelope was accreted from the disk.

We generate synthetic transmission and emission spectra for all our atmospheric disequilibrium chemistry outputs and find that differences in the chemistry manifest clearly in different spectral signatures of H_2O, CH_4, HCN, and CO in both types of spectra. Transmission spectra for almost all chemistry outputs are full of features and are broadly divided into three types: majority H_2O, majority CH_4, and majority HCN-CN. We then compare the species that were validated in the atmosphere of HD 209458b to the spectral fingerprints of our plots and found that this requirement could possibly be satisfied by spectra from four model cases: B1/B2 and F1/F2. These correspond to cases of gas accretion between the CO_2 and CH_4 ice lines for both low and high ionizations for inverted and noninverted P–T profiles, respectively. Most of the other models with similar molecular detections are too depleted in elemental abundances compared to observations from Giacobbe et al. (2021). Our results are in agreement with the result of Giacobbe et al. (2021) as well as with that of Hobbs et al. (2021b). However, we also find that contamination by disk solids can induce a massive change in the spectra by changing the C/O values of the envelope. Judging the extent of this contamination is very model dependent and can vary depending on whether one assumes molecular or atomic initial abundances. It also depends on whether the disk model is static or evolving. Hence, while we obtain a possible formation location using a simplified scenario, we defer the use of such model-dependent cases to judge the true extent of change due to disk solid contamination for future works.

Finally, we simulated observing our model atmospheres with the JWST instruments NIRCam and MIRI LRS at wavelengths 2.4–13 μm and detect the fingerprints of several species, and we find that we can distinguish between the three main spectrum types found in our simulations, i.e., majority H_2O, majority CH_4, and majority HCN(+CN). This shows that investigating the formation histories of hot Jupiters through their atmospheric compositions will be viable with the JWST and will provide valuable insights into the formation environments of exoplanets.

Software: VULCAN (Tsai et al. 2017, 2021), petitRADTRANS (Mollière et al. 2019), HELIOS (Malik et al. 2017) and PandExo (Batalha et al. 2017).

Appendix

Table 3 shows the main reaction pathways for CH4-C2H2, CH4-CO, CH4-HCN, NH3-HCN, and N2-NH3 conversions at a pressure level of 1 mbar for various models listed in Table 1. Figures 12–16 shows the various types of reaction pathways for CH4-C2H2, CH4-CO, CH4-HCN, NH3-HCN, and N2-NH3 conversions possible in our models.

Table 3
Model-wise Distribution of Reaction Pathways (Type is Denoted by a Numerical Value) at $P = 1$ mbar

Model	CH_4–C_2H_2 scheme	CH_4–CO scheme	CH_4–HCN scheme	NH_3–HCN scheme	N_2–NH_3 scheme	C/O
A1/A2	1/3	1/1	1/1	2/2	1/2	0.35
B1/B2	2/5	1/2	1/1	2/2	1/1	0.81
C1/C2	2/5	1/2	1/1	2/2	1/1	1.27
D1/D2	2/5	1/2	1/1	2/2	1/1	1.00
E1/E2	1/3	1/1	1/1	2/2	1/2	0.35
F1/F2	2/5	1/2	1/1	2/2	1/1	0.82
G1/G2	2/5	1/2	1/1	2/2	1/1	0.94
H1/H2	2/2	1/3	1/1	2/2	1/1	1.00
I1/I2	1/3	1/1	1/1	2/2	1/2	0.35
J1/J2	1/3	1/1	1/1	2/2	1/2	0.35
K1/K2	1/4	1/1	1/2	2/1	1/2	0.13
L1/L2	2/2	1/1	1/1	2/2	1/1	0.41
M1/M2	1/3	1/1	1/1	2/2	1/2	0.35
N1/N2	1/3	1/1	1/1	2/2	1/2	0.35
O1/O2	1/4	1/1	1/2	2/1	1/2	0.25
P1/P2	2/2	1/2	1/1	2/2	1/1	0.89

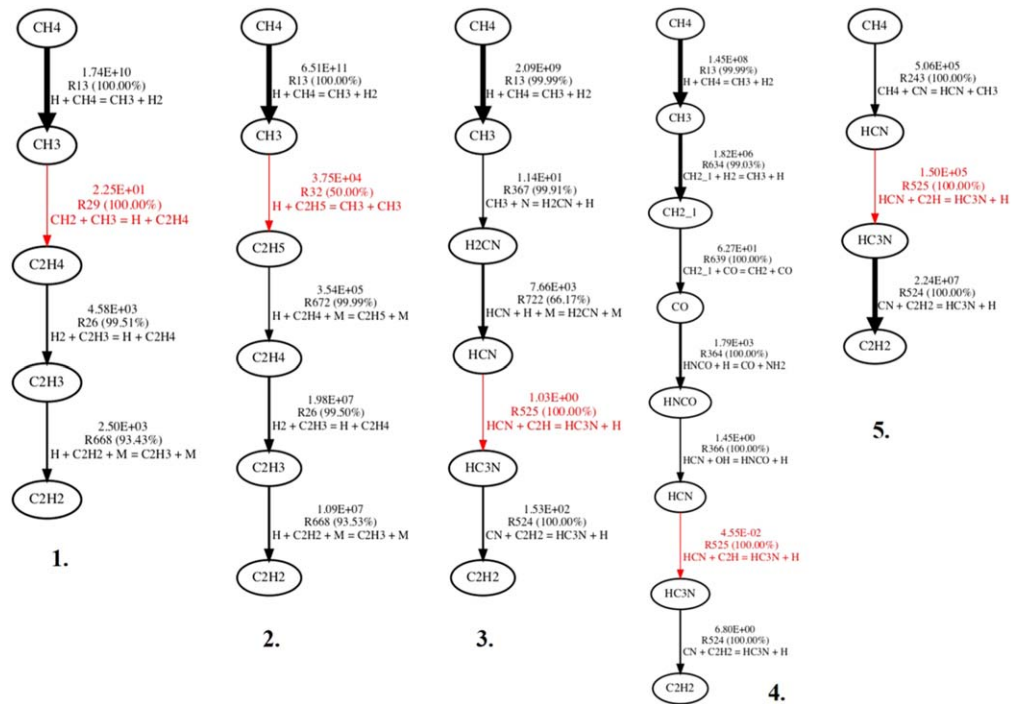**Note.** The numerical values for the reaction pathway types are labeled in Figures 12, 13, 14, 15, and 16.

Figure 12. Examples of the types of CH$_4$–C$_2$H$_2$ reaction pathways possible in our models. Thicker lines represent faster reaction rates, which are denoted by the first-row numbers shown in cm^{-3} s^{-1}, and the red lines are the rate-limiting steps. RX denotes the reaction number from the VULCAN reaction network. An odd RX shows a forward reaction, and an even RX shows the opposite. The percentage of the contribution to the interconversion is also provided. The values of the rates and percentages will change from model to model, while the pathway denoted by a number (below each) is representative.
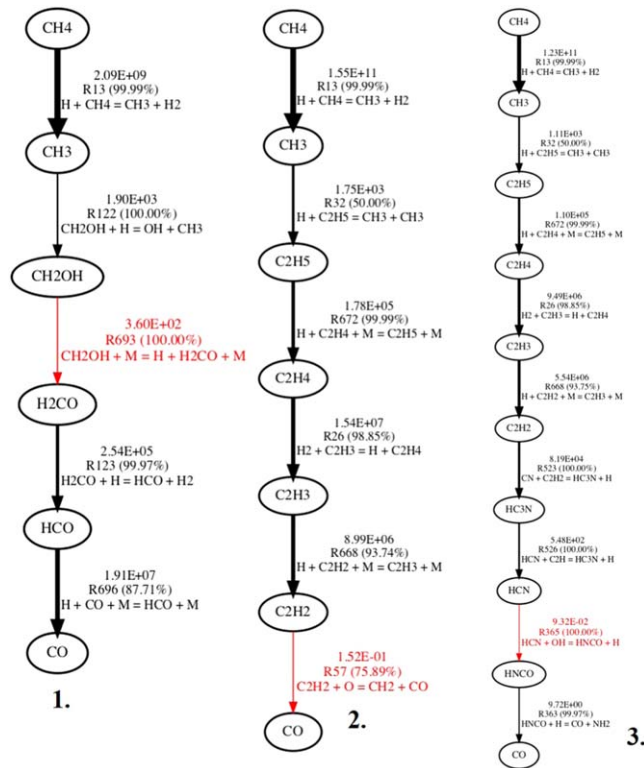
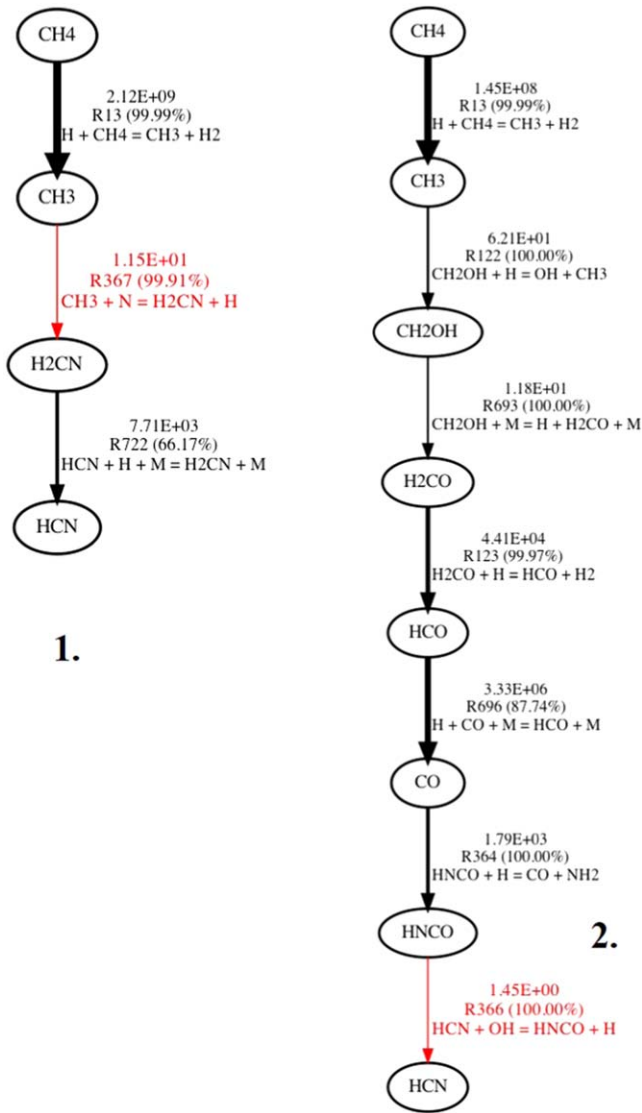**Figure 13.** Same as Figure 12, but for the CH$_4$–CO reaction.

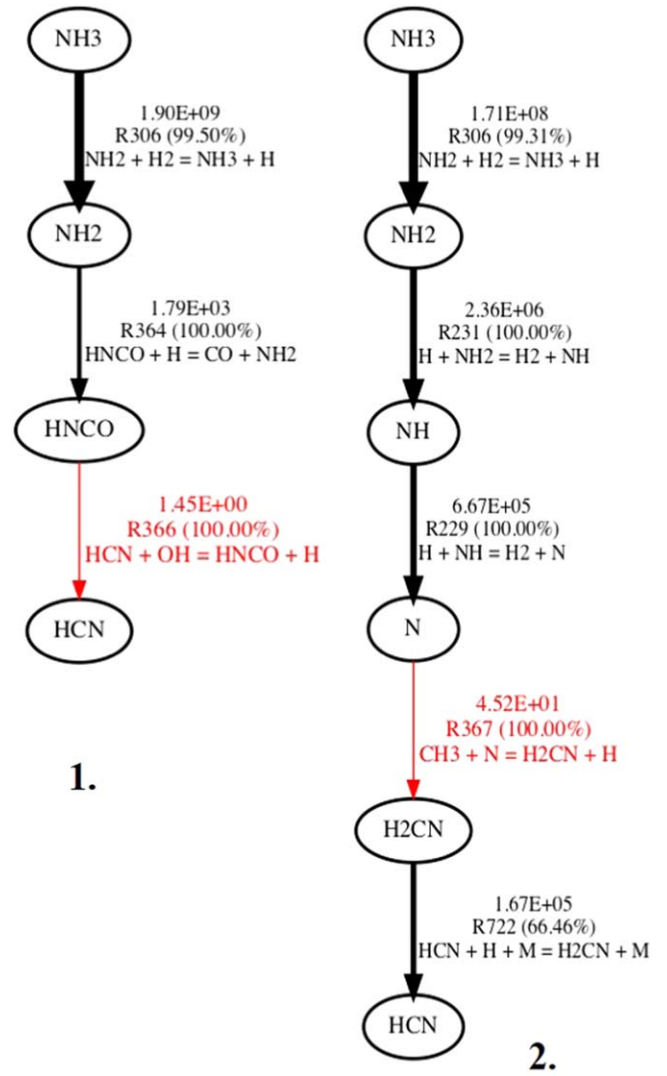**Figure 14.** Same as Figure 12, but for the CH$_4$–HCN reaction.

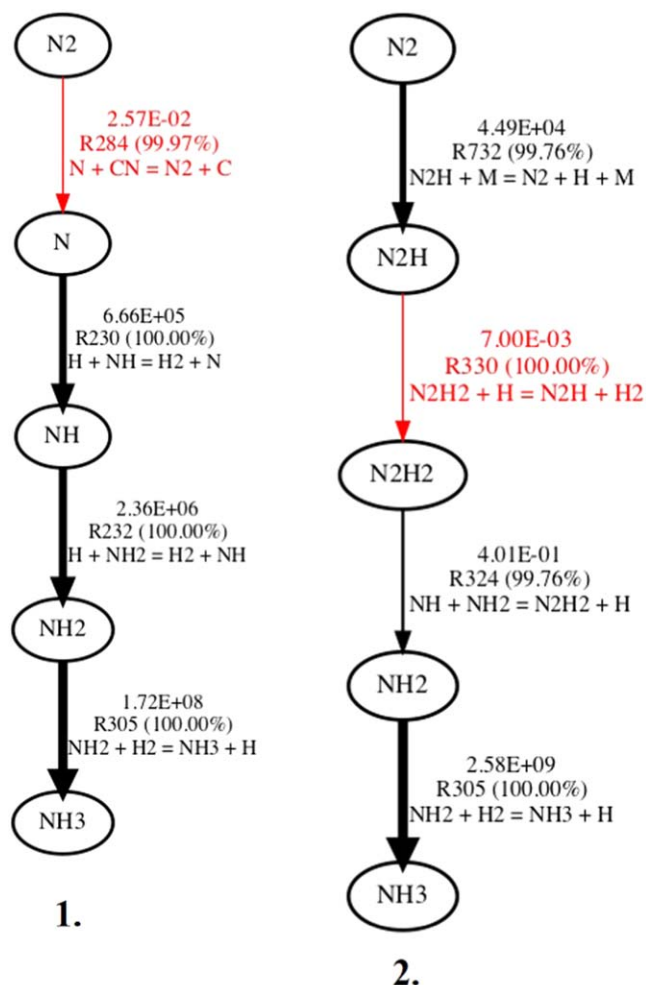**Figure 15.** Same as Figure 12, but for the NH$_3$–HCN reaction.

Figure 16. Same as Figure 12, but for the N_2–NH_3 reaction.

ORCID iDs

Spandan Dash ● https://orcid.org/0000-0003-3652-3690
Liton Majumdar ● https://orcid.org/0000-0001-7031-8039
Karen Willacy ● https://orcid.org/0000-0001-6124-5974
Shang-Min Tsai ● https://orcid.org/0000-0002-8163-4608
Neal Turner ● https://orcid.org/0000-0001-8292-1943
P. B. Rimmer ● https://orcid.org/0000-0002-7180-081X
Murthy S. Gudipati ● https://orcid.org/0000-0001-5992-373X
Wladimir Lyra ● https://orcid.org/0000-0002-3768-7542
Anil Bhardwaj ● https://orcid.org/0000-0003-1693-453X

References

Alibert, Y., Venturini, J., Helled, R., et al. 2018, NatAs, 2, 873
Ali-Dib, M. 2017, MNRAS, 467, 2845
Amundsen, D. S., Baraffe, I., Tremblin, P., et al. 2014, A&A, 564, A59
Appelgren, J., Lambrechts, M., & Johansen, A. 2020, A&A, 638, A156
Asplund, M., Grevesse, N., Sauval, A. J., & Scott, P. 2009, ARA&A, 47, 481
Batalha, N. E., Mandell, A., Pontoppidan, K., et al. 2017, PASP, 129, 064501
Blecic, J., Harrington, J., & Bowman, M. O. 2016, ApJS, 225, 4
Booth, R. A., & Ilee, J. D. 2019, MNRAS, 487, 3998
Boyajian, T., von Braun, K., Feiden, G. A., et al. 2015, MNRAS, 447, 846
Brogi, M., & Line, M. R. 2019, AJ, 157, 114
Brown, T. M. 2001, ApJ, 553, 1006
Burrows, A., Hubeny, I., Budaj, J., Knutson, H., & Charbonneau, D. 2007, ApJL, 668, L171
Charbonneau, D., Brown, T. M., Noyes, R. W., & Gilliland, R. L. 2002, ApJ, 568, 377
Cridland, A., Pudritz, R. E., Birnstiel, T., Cleeves, L. I., & Bergin, E. A. 2017, MNRAS, 469, 3910
Cridland, A. J., Bosman, A. D., & van Dishoeck, E. F. 2020, A&A, 635, A68
Cridland, A. J., Eistrup, C., & van Dishoeck, E. F. 2019a, A&A, 627, A127
Cridland, A. J., van Dishoeck, E. F., Alessi, M., & Pudritz, R. E. 2019b, A&A, 632, A63
Dash, S., & Miguel, Y. 2020, MNRAS, 499, 3510
Diamond-Lowe, H., Stevenson, K. B., Bean, J. L., Line, M. R., & Fortney, J. J. 2014, ApJ, 796, 66
Drummond, B., Tremblin, P., Baraffe, I., et al. 2016, A&A, 594, A69
Eistrup, C., Walsh, C., & Van Dishoeck, E. F. 2016, A&A, 595, A83
Eistrup, C., Walsh, C., & van Dishoeck, E. F. 2018, A&A, 613, A14
Giacobbe, P., Brogi, M., Gandhi, S., et al. 2021, Natur, 592, 205
Guillot, T. 2010, A&A, 520, A27
Hobbs, R., Rimmer, P., Shorttle, O., & Madhusudhan, N. 2021a, MNRAS, 506, 3186
Hobbs, R., Shorttle, O., & Madhusudhan, N. 2021b, arXiv:2112.04930
Hobbs, R., Shorttle, O., Madhusudhan, N., & Rimmer, P. 2019, MNRAS, 487, 2242
Hubbard, W. B., Fortney, J., Lunine, J., et al. 2001, ApJ, 560, 413
Knutson, H. A., Charbonneau, D., Allen, L. E., Burrows, A., & Megeath, S. T. 2008, ApJ, 673, 526
Komacek, T. D., & Showman, A. P. 2016, ApJ, 821, 16
Kopparapu, R. K., Kasting, J. F., & Zahnle, K. J. 2012, ApJ, 745, 77
Lavvas, P., & Arfaux, A. 2021, MNRAS, 502, 5643
Liang, M.-C., Parkinson, C. D., Lee, A. Y.-T., Yung, Y. L., & Seager, S. 2003, ApJL, 596, L247
Line, M. R., Stevenson, K. B., Bean, J., et al. 2016, AJ, 152, 203
MacDonald, R. J., & Madhusudhan, N. 2017, MNRAS, 469, 1979
Malik, M., Grosheintz, L., Mendonça, J. M., et al. 2017, AJ, 153, 56
Manara, C. F., Morbidelli, A., & Guillot, T. 2018, A&A, 618, L3
Miguel, Y., Cridland, A., Ormel, C., Fortney, J., & Ida, S. 2020, MNRAS, 491, 1998
Mollière, P., Wardenier, J., van Boekel, R., et al. 2019, A&A, 627, A67
Morbidelli, A., Szulágyi, J., Crida, A., et al. 2014, Icar, 232, 266
Mordasini, C., van Boekel, R., Mollière, P., Henning, T., & Benneke, B. 2016, ApJ, 832, 41
Moses, J. I. 2014, RSPTA, 372, 20130073
Moses, J. I., Line, M. R., Visscher, C., et al. 2013a, ApJ, 777, 34
Moses, J. I., Madhusudhan, N., Visscher, C., & Freedman, R. S. 2013b, ApJ, 763, 25
Moses, J. I., Visscher, C., Fortney, J. J., et al. 2011, ApJ, 737, 15
Notsu, S., Eistrup, C., Walsh, C., & Nomura, H. 2020, MNRAS, 499, 2229
Nowak, M., Lacour, S., Mollière, P., et al. 2020, A&A, 633, A110
Öberg, K. I., Murray-Clay, R., & Bergin, E. A. 2011, ApJL, 743, L16
Pollack, J. B., Hubickyj, O., Bodenheimer, P., et al. 1996, Icar, 124, 62
Rimmer, P. B., & Helling, C. 2016, ApJS, 224, 9
Sánchez-López, A., Alonso-Floriano, F. J., López-Puertas, M., et al. 2019, A&A, 630, A53
Seager, S., & Sasselov, D. 2000, ApJ, 537, 916
Sing, D. K., Fortney, J. J., Nikolov, N., et al. 2016, Natur, 529, 59
Snellen, I. A., De Kok, R. J., De Mooij, E. J., & Albrecht, S. 2010, Natur, 465, 1049
Southworth, J. 2010, MNRAS, 408, 1689
Stock, J. W., Kitzmann, D., Patzer, A. B. C., & Sedlmayr, E. 2018, MNRAS, 479, 865
Swain, M. R., Tinetti, G., Vasisht, G., et al. 2009, ApJ, 704, 1616
Tanigawa, T., Ohtsuki, K., & Machida, M. N. 2012, ApJ, 747, 47
Teague, R., Bae, J., & Bergin, E. A. 2019, Natur, 574, 378
Tsai, S.-M., Kitzmann, D., Lyons, J. R., et al. 2018, ApJ, 862, 31
Tsai, S.-M., Lyons, J. R., Grosheintz, L., et al. 2017, ApJS, 228, 20
Tsai, S.-M., Malik, M., Kitzmann, D., et al. 2021, ApJ, 923, 264
Tsiaras, A., Waldmann, I., Rocchetto, M., et al. 2016, ApJ, 832, 202
Tsiaras, A., Waldmann, I., Zingales, T., et al. 2018, AJ, 155, 156
Turrini, D., Schisano, E., Fonte, S., et al. 2021, ApJ, 909, 40
Venot, O., Hébrard, E., Agúndez, M., et al. 2012, A&A, 546, A43
Vidal-Madjar, A., Des Etangs, A. L., Désert, J.-M., et al. 2003, Natur, 422, 143
Vidal-Madjar, A., Désert, J.-M., Des Etangs, A. L., et al. 2004, ApJL, 604, L69
Visser, R., Bergin, E. A., & Jørgensen, J. K. 2015, A&A, 577, A102
Wenger, M., Ochsenbein, F., Egret, D., et al. 2000, A&AS, 143, 9
Woitke, P., Kamp, I., & Thi, W.-F. 2009, A&A, 501, 383
Zahnle, K., Marley, M. S., Freedman, R. S., Lodders, K., & Fortney, J. 2009, ApJL, 701, L20
Zilinskas, M., Miguel, Y., Mollière, P., & Tsai, S.-M. 2020, MNRAS, 494, 1490